

Properties and geoeffectiveness of solar wind high-speed streams and stream interaction regions during solar cycles 23 and 24

Maxime Grandin^{1,2}, Anita T. Aikio³, and Alexander Kozlovsky¹

¹Sodankylä Geophysical Observatory, University of Oulu, Sodankylä, Finland

²Department of Physics, University of Helsinki, Helsinki, Finland

³Ionospheric Physics Unit, University of Oulu, Oulu, Finland

Key Points:

- Stream interaction regions and high-speed streams (SIR/HSSs) are 20–40% less geoeffective during solar cycle (SC) 24 than during SC23
- The most geoeffective SIR/HSSs in solar cycles 23 and 24 take place in the early declining phases
- During the late declining phase of SC23, both SIR/HSS event number and maximum velocity are highest, yet their geoeffectiveness is low

arXiv:2006.06302v1 [physics.space-ph] 11 Jun 2020

Corresponding author: Maxime Grandin, maxime.grandin@helsinki.fi

Abstract

We study the properties and geoeffectiveness of solar wind high-speed streams (HSSs) emanating from coronal holes and associated with stream interaction regions (SIRs). This paper presents a statistical study of 588 SIR/HSS events with solar wind speed at 1 AU exceeding 500 km/s during 1995–2017, encompassing the decline of solar cycle 22 to the decline of cycle 24. Events are detected using measurements of the solar wind speed and the interplanetary magnetic field (IMF). Events misidentified as or interacting with interplanetary coronal mass ejections (ICMEs) are removed by comparison with an existing ICME list. Using this SIR/HSS event catalog (list given in the supplementary material), a superposed epoch analysis of key solar wind parameters is carried out. It is found that the number of SIR/HSSs peaks during the late declining phase of solar cycle (SC) 23, as does their velocity, but that their geoeffectiveness in terms of the *AE* and *SYM-H* indices is low. This can be explained by the anomalously low values of magnetic field during the extended solar minimum. Within SC23 and SC24, the highest geoeffectiveness of SIR/HSSs takes place during the early declining phases. Geoeffectiveness of SIR/HSSs continues to be up to 40% lower during SC24 than SC23, which can be explained by the solar wind properties.

1 Introduction

Corotating solar wind high-speed streams (HSSs) were discovered by *Snyder et al.* [1963], who showed a correlation between recurring geomagnetic activity and the solar wind speed measured by Mariner 2. High-speed streams were later associated with solar coronal holes [e.g., *Krieger et al.*, 1973; *Sheeley Jr et al.*, 1976]. Since a given coronal hole may persist for several solar rotations, this will lead to recurring geomagnetic activity with a ~27-day period in many parameters in the atmosphere, ionosphere, and magnetosphere [e.g., *Chkhetia*, 1975; *Hapgood*, 1993; *Temmer et al.*, 2007; *Crowley et al.*, 2008], this periodicity corresponding to the synodic solar rotation period as viewed from Earth. A HSS is characterized by an enhancement in the solar wind velocity lasting for several days. Typically, the speed exceeds 500 km/s for two to three days, and may reach a maximum above 800 km/s [e.g., *Denton and Borovsky*, 2012; *Kavanagh et al.*, 2012].

When the high-speed stream overtakes the slow-speed background stream, this leads to compressions of both the interplanetary magnetic field (IMF) and the plasma density in the rising-speed portion of the high-speed stream [*Belcher and Davis*, 1971]. The resulting structure was called corotating interaction region (CIR) [*Smith and Wolfe*, 1976; *Gosling and Pizzo*, 1999]. In this paper, we refer to this interaction region as “stream interaction region (SIR)” regardless of the number of solar rotations during which it is observed. This practice is similar to, e.g., *Richardson* [2018]. In addition, the high-speed stream events that we study contain the interaction regions in the leading edge of the streams, so we refer to these events as SIR/HSS.

SIR/HSSs have been particularly studied during the declining phase of the 11-year solar cycle, since at that time they represent the main cause for geomagnetic disturbances [*Gonzalez et al.*, 1999; *Tsurutani et al.*, 2006]. On the other hand, during the maximum years of solar activity, coronal mass ejections (CMEs) are the major cause of geomagnetic disturbances [e.g., *Richardson and Cane*, 2012a]. CMEs are eruptions of magnetized plasma from the solar atmosphere, with a broad range of propagation speeds [*Gopalswamy and Kundu*, 1992]. Interplanetary coronal mass ejections (ICMEs) are the interplanetary counterpart of CMEs [e.g., *Schwenn*, 1983; *Sheeley et al.*, 1985; *Lindsay et al.*, 1999; *Webb et al.*, 2000]. Those produce the most extreme space weather events [e.g., *Richardson et al.*, 2000, 2001; *Zhang et al.*, 2007; *Echer et al.*, 2013].

It is well-established that SIR/HSSs are predominantly responsible for weak to moderate geomagnetic storms [e.g., *Tsurutani et al.*, 2006]. *Zhang et al.* [2008] found that about 80% of the geomagnetic storms produced by “pure” SIR/HSSs (i.e., SIR/HSSs which are not interacting with an ICME) are weak ($-50 < Dst \leq -30$ nT) to moderate ($-100 <$

$Dst \leq -50$ nT), while *Alves et al.* [2006] showed that only about 33% of the SIR/HSSs are responsible for moderate to intense storms ($Dst \leq -100$ nT). *Chi et al.* [2018] found that a large fraction of the most intense SIR/HSS-related geomagnetic storms are produced by SIR/HSSs interacting with an ICME. According to *Kilpua et al.* [2017], although SIR/HSSs are frequent during solar minimum, they produce fewer geomagnetic storms as they are generally characterized with lower speed gradients, lower dynamical pressure peaks and lower interplanetary magnetic field magnitude. Yet, *Richardson and Cane* [2012a] revealed that almost half of the large storms during solar minimum are due to SIR/HSSs.

Statistical studies of SIR/HSS effects on the magnetosphere–ionosphere–thermosphere system have shown dropouts of relativistic electrons in the outer radiation belt [*Borovsky and Denton*, 2009; *Morley et al.*, 2010], followed by a recovery to higher flux levels in the case of strong events [*Denton and Borovsky*, 2012], enhancement of substorm activity [*Tsurutani et al.*, 2006], depletion of the ionospheric *F* region [*Denton et al.*, 2009; *Grandin et al.*, 2015], energetic ($E > 30$ keV) electron precipitation into the *D* region [*Meredith et al.*, 2011; *Grandin et al.*, 2017], and enhancement of ULF wave activity in the magnetosphere [*Mathie and Mann*, 2001].

Because of the strong influence of SIR/HSS events on the planetary environment, objective criteria to identify SIR/HSS events from solar wind data would be very useful. Previous statistical studies have used methods to detect SIR/HSSs focusing on stream interfaces, and hence searching for not only enhancement in the solar wind radial velocity but also a west–east deflection of the plasma flow [e.g., *Morley et al.*, 2010; *Denton and Borovsky*, 2012; *Kavanagh et al.*, 2012]. Those methods often required a visual inspection of the events and/or comparison with existing lists of other solar wind disturbances such as ICMEs to remove false positives. For instance, *Jian et al.* [2006] produced a fairly comprehensive list of events during 1995–2004, which was extended till the end of 2016 by *Chi et al.* [2018]. The events were picked by eye based on criteria on the solar wind speed and total perpendicular pressure. The starting time corresponds to the time when the total perpendicular pressure starts increasing, which is close to the time when the speed also starts increasing. *Richardson and Cane* [2012b] have also produced a classification of solar wind flows, including an identification of SIR/HSSs, during 1963–2011 based on visual inspection of solar wind data as well as geomagnetic observations, energetic particle data, and neutron monitor data. Others have developed automated methods using only criteria related to the enhancement of the solar wind speed, such as *Mariş Muntean et al.* (<http://www.geodin.ro/varsiti/>) during 2009–2016 or *Gupta and Badruddin* [2010] during 1996–2007.

More generally, attempts to automatically identify solar wind flow types between inter-stream flow (slow wind), coronal-hole flow (high-speed streams), and transient (ICMEs) have been presented by, e.g., *Zhao et al.* [2009] during 1998–2008 from ACE data, *Reisenfeld et al.* [2013] during the Genesis mission (2001–2004), and *Xu and Borovsky* [2015] during 1963–2013 from OMNI data. However, when comparing results from the latter three identification schemes, *Neugebauer et al.* [2016] found that the overall agreement is limited, with all three algorithms giving a same flow type only 49% of the time.

This paper presents a method to identify SIR-associated HSSs, which is applied to 23 years of solar wind observations from 1995 until 2017. This detection method is based on the one used to obtain the HSS events analyzed in *Grandin et al.* [2015, 2017] for 2006–2008, and for this paper some improvements have been developed, detailed in section 3. The aim of this method is to find the time when the SIR region with compressed magnetic field hits the bow shock. Solar wind speed reaches the maximum typically 1–2 days after this zero epoch. It was shown in *Grandin et al.* [2015, 2017] that the zero epoch selected in this manner corresponds very well to the time when geomagnetic activity in terms of the AE index starts to increase. The list of SIR/HSSs obtained with this new algorithm is used to self-consistently study the features of SIR/HSSs impinging on the Earth’s magnetopause during the different phases of two solar cycles, and in specific their geoeffectiveness.

This paper is organized as follows: the data sets used in this study are presented in section 2, and the algorithm developed to gather the list of SIR/HSS events is described in section 3. Section 4 presents the results on SIR/HSS characteristics from the end of solar cycle 22 (SC22) until late 2017 (declining phase of SC24). Section 5 discusses the results and compares the obtained SIR/HSS list with other existing ones, and section 6 summarizes the main conclusions.

2 Data

The data used in this study consist of interplanetary magnetic field (IMF) and solar wind data measured near the Earth between 1995 and 2017. The data were obtained by several satellites of which the main ones are WIND (1995–present) [Ogilvie *et al.*, 1995] and ACE (1998–present) [McComas *et al.*, 1998; Smith *et al.*, 1998]. The measured data are available through the OMNI database [King and Papitashvili, 2005], where they have already been propagated to the terrestrial bow shock. The parameters of interest in this study are the IMF magnitude B , the solar wind speed V , the solar wind density N , and the Akasofu ε parameter [Akasofu, 1979] calculated using

$$\varepsilon = \frac{4\pi}{\mu_0} V B^2 L_0^2 \sin^4 \left(\frac{\theta}{2} \right), \quad (1)$$

with μ_0 the vacuum permeability, θ the IMF clock angle in the plane perpendicular to the Sun–Earth direction, and $L_0 \simeq 7R_E$. The Akasofu ε parameter is a coupling function often used as a proxy for energy input from the solar wind into the magnetosphere. For this study, the OMNI data were retrieved for years 1995–2017 at 1 h time resolution.

We also take the 1–h averages of the auroral electrojet (*AE*) and *SYM-H* geomagnetic indices [Davis and Sugiura, 1966; Iyemori, 1990] from OMNI to monitor the response of the geospace in terms of substorm and storm activity, respectively.

In addition, in order to discuss the properties of SIR/HSSs during different phases of solar cycles 23 and 24, the monthly values of the revised sunspot number between 1995 and 2017 have been gathered from the World Data Center Sunspot Index and Long-Term Solar Observations (SILSO) [SILSO World Data Center, 1995-2017].

3 SIR/HSS Event Detection Algorithm

Our aim is to find SIR/HSS events that can be geoeffective. Therefore, for maximum velocity we have chosen a threshold of 500 km/s. One can see that the Akasofu epsilon solar wind coupling function (eq. 1) depends linearly on solar wind velocity. The papers by Kavanagh *et al.* [2012] and Denton and Borovsky [2012] are also in accordance with this selection, see point 2(c) below. However, the algorithm presented below could be adapted to also detect SIR/HSSs of lower maximum speed.

The algorithm used to detect SIR/HSS events for this study consists of four steps. The first three steps each consider a criterion based on solar wind data at 1 h resolution provided by OMNI.

1. The SIR is formed by the plasma compression arising from the interaction of the slow and fast solar wind streams. Therefore the leading edge of SIRs exhibits an enhancement in the IMF magnitude B [e.g., Richter and Luttrell, 1986; McPherron and Weygand, 2006; Denton and Borovsky, 2012]. Hence, as a first criterion, the time derivative of B is estimated at each time t_i using

$$\frac{dB}{dt} \simeq \frac{1}{2\Delta t} (B_{i+1} - B_{i-1}), \quad (2)$$

with $\Delta t = t_{i+1} - t_i = 1$ h the time resolution of the solar wind data. Each instant t_i at which this time derivative value exceeds the empirically determined threshold

- of 0.6 nT/h is then flagged as a candidate SIR/HSS event starting time (t_0). If the threshold value is too large, only SIRs that are associated with a forward shock will be detected. *Jian et al.* [2006] found that, on average, the occurrence rate of forward shocks in SIRs at 1 AU is about 18%. However, if the threshold value is too small, then we are no more looking at compressed plasma, but some natural fluctuations in B. The threshold value used in this paper was found empirically, and comparison to other existing SIR lists described in Section 5.1 shows that the threshold works well, since no events are missed due to this criterion.
2. The second criterion is based on the solar wind velocity V . The candidate events obtained with criterion (1) are tested for three characteristics:
 - (a) To avoid detecting events taking place while the background solar wind speed is already high, at time t_0 , one must have $V(t_0) \leq 450$ km/s, bearing in mind that occasional compound events consisting of two high-speed streams interacting with each other might not be detected due to this restriction. This value of 450 km/s was also determined empirically by visual inspection of the detected/undetected SIR/HSS events when trying various velocity thresholds.
 - (b) To ensure that the velocity starts increasing shortly after the beginning of the event, the average velocity slope between t_0 and t_0+1 day must be greater than 30 (km/s)/day, which is consistent with definitions of HSSs adopted by *Bame et al.* [1976] and *Gosling et al.* [1976].
 - (c) To keep only events with solar wind speed significantly higher than the slow wind, a threshold is defined: the solar wind speed must reach at least 500 km/s within $[t_0, t_0 + 3 \text{ days}]$. This value of 500 km/s is the same as used by *Kavanagh et al.* [2012] in their superposed epoch study of >30 keV precipitation during high-speed streams, and falls between the thresholds defined by *Denton and Borovsky* [2012] for “weak” (450 km/s) and “strong” (550 km/s) HSS events. It is also consistent with the retained velocity thresholds used for the detection of coronal-hole flow by the Genesis spacecraft mission [*Reisenfeld et al.*, 2013].

The candidate SIR/HSS event starting times which verify each of those three conditions are kept for the next step.

3. The third criterion makes sure that one does not detect a same SIR/HSS event twice when, for instance, criteria (1) and (2) are met at several times during the event. Criterion (3) consists in keeping only SIR/HSS event starting times separated by at least 3 days. Beginning with the first detected SIR/HSS event at t_0 , all candidate times between t_0 and $t_0 + 3$ days are examined, and the one associated with the lowest solar wind speed, at time t'_0 , is retained while all others are removed from the list. This guarantees that the solar wind speed starts increasing immediately after the retained starting time. This operation is repeated for the next SIR/HSS candidate occurring after $t'_0 + 3$ days, and so on until the end of the list of candidates is reached.

When applied to the solar wind data collected between 1 January 1995 and 31 December 2017, these three criteria lead to the detection of 709 candidate SIR/HSS events. However, some of these events are not purely SIR-related HSSs.

4. The list of candidates is then compared to the list of near-Earth ICMEs provided by *Richardson and Cane* [2010], which covers years from 1996 onward and is regularly updated (<http://www.srl.caltech.edu/ACE/ASC/DATA/level3/icmetable2.htm>). A candidate is considered a likely ICME or contaminated by an ICME if one event from the Richardson and Cane list with $V_{\max} \geq 500$ km/s reached the Earth between $t_0 - 1$ day and $t_0 + 3$ days, t_0 being the date of the candidate SIR/HSS event.

In total, 122 events matching criterion 4 were found and were removed from the SIR/HSS catalogue. As a consequence, this leaves a total of 588 SIR/HSS events obtained with this four-step method. This list of SIR/HSS events is provided as supporting information. The list

gives for each SIR/HSS event its starting time t_0 , initial solar wind speed, the time and value of maximum solar wind speed during $[t_0, t_0+3 \text{ days}]$, and an end time defined as the first occurrence when the solar wind speed drops below 450 km/s after reaching its maximum. All times are given in UT for solar wind propagated at the terrestrial bow shock as given in OMNI. It should be noted that this list does not claim to be comprehensive, as (i) this study focuses on SIR/HSS events whose velocity reaches at least 500 km/s, (ii) occasionally, some SIR/HSS events with $V_{\max} \geq 500 \text{ km/s}$ might have been undetected by the method, and (iii) events containing ICMEs during $[t_0 - 1 \text{ day}, t_0 + 3 \text{ days}]$ are removed.

Figure 1 illustrates some aspects of the detection algorithm on solar wind data gathered in June 2008. During this time window, four SIR/HSS events were detected by the algorithm. Their starting times are 6 June at 4 UT, 14 June at 12 UT, 19 June at 20 UT, and 24 June at 20 UT, and those are indicated by vertical dashed lines and the ticks on the x -axis. Figure 1a shows the solar wind speed. It is clear that the beginning of each event is set very close to the time when the solar wind velocity starts to increase, which naturally comes from criteria 2b and 3. The horizontal red dashed line indicates the threshold value at 500 km/s for a HSS event (criterion 2c). Figure 1b gives the IMF magnitude $|B|$ which is used for criterion 1. The sharp time derivative used for the detection is particularly prominent at the beginning of the second event. From Figure 1c, which shows the solar wind number density, it can be noted that the beginning of the detected SIR/HSS events is close to the maximum of the density peak (again, this is more prominent for the second event), which corresponds to earlier findings [e.g., *Gosling et al.*, 1972; *McPherron and Weygand*, 2006; *Denton et al.*, 2009]. Figure 1d displays the *AE* index, which is a proxy for substorm activity [*Iyemori*, 1990]. Substorm activity starts to increase very close to the determined onset time of the events in each case. It is interesting to note that *AE* starts to increase well before the solar wind velocity has reached a high value, which indicates that the SIR is geoeffective. Figure 1e displays the *SYM-H* index, which describes the intensity of the storm time ring current [*Wanliss and Showalter*, 2006]. In the 14 June event, which is associated with the strongest storm, the zero epoch matches very well with the sudden storm commencement signature showing as a positive peak in *SYM-H*, likely to be produced by the slight dayside magnetopause compression associated with the SIR arrival. A smaller positive peak is observed also for the other events, except the first one on 6 June. All these events are associated with weak magnetic storms. It is well-known that SIR-associated geomagnetic storms are frequent in the declining phase of the solar cycle and are typically weak to moderate [*Tsurutani et al.*, 2006; *McPherron and Weygand*, 2006; *Richardson and Cane*, 2012a; *Grandin et al.*, 2017].

Figure 2 shows the same data as Figure 1 but for the whole year 2008, during which 33 SIR/HSS events were detected by the algorithm. From this longer time series, the features described above can be identified in most of the detected events, namely the fact that the beginning of events corresponds well with the start of the solar wind speed increase, with a peak in the solar wind density within the SIR region, with the start of *AE* index enhancement, and is near the sudden storm commencement signature when it is present. One can note that the event contaminated by the only ICME with $V_{\max} \geq 500 \text{ km/s}$ in 2008, which took place on 4 December (magenta triangle in Figure 2a), was rejected by the algorithm because of criterion 4.

Figure 3 gives the yearly distribution of ICMEs with $V_{\max} \geq 500 \text{ km/s}$ from the Richardson and Cane list between 1996 and 2017 (the envelope of the histogram). Orange bars show the ICME events that were identified as SIR/HSSs by our algorithm with steps 1–3, before they were removed based on criterion 4, and blue bars show the remaining ICME events. The black line gives the monthly sunspot number during those years. It is noteworthy that not all the ICMEs are misidentified as SIR/HSSs by our algorithm, only 122 out of 237 ICMEs with speeds larger than 500 km/s, corresponding to about 50%. Of all the detected SIR/HSS events, the amount of rejected events (ICMEs or SIR/HSSs contaminated by ICMEs) is 17% (122/709). This underlines the fact that comparison with an ICME list (criterion 4) is a necessary step in the algorithm, as the solar wind parameters used in the identification scheme

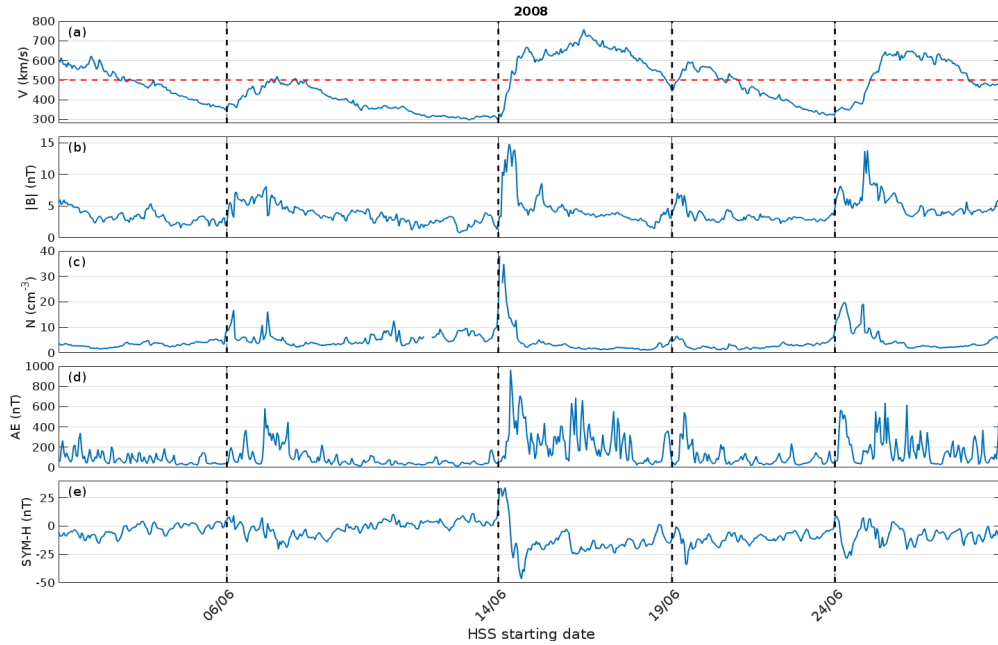


Figure 1. SIR/HSS events detected by the algorithm in June 2008 with a maximum solar wind velocity greater than 500 km/s. Each vertical dashed line corresponds to the beginning of an event. The time series shown are (a) the solar wind velocity, (b) the IMF magnitude, (c) the solar wind number density, (d) the AE index, and (e) the *SYM-H* index. The horizontal dashed red line in the first panel indicates $V = 500$ km/s, used for criterion 2(c).

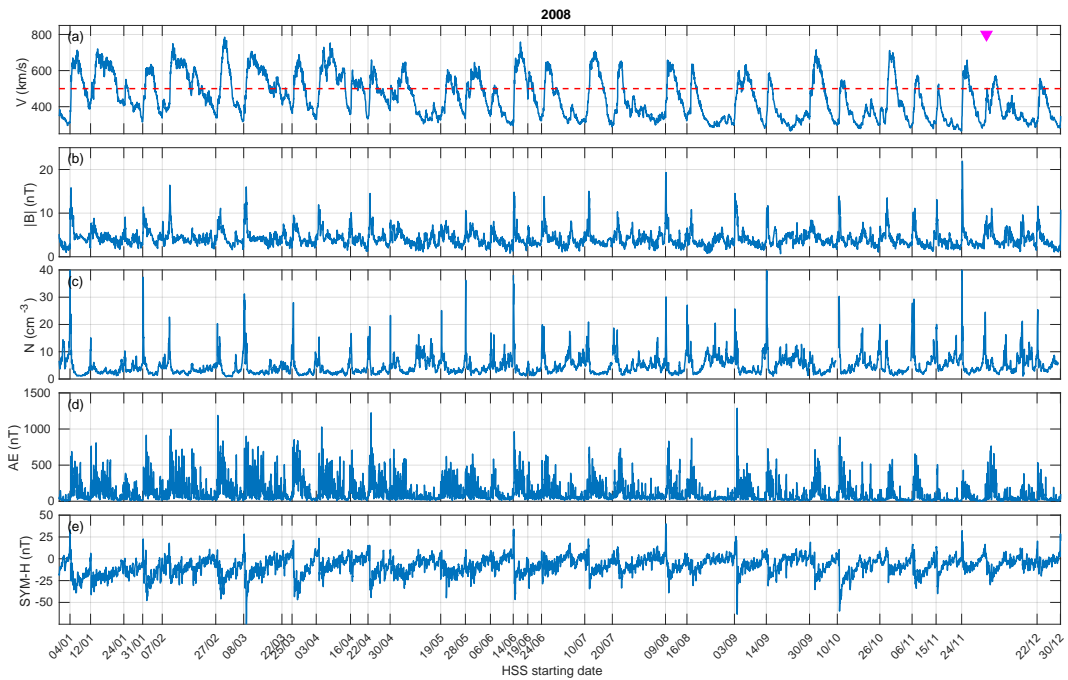


Figure 2. Same as Figure 1 but showing the data and detected events for the entire year 2008. The magenta triangle in panel (a) corresponds to the ICME falsely detected as SIR/HSS in 2008, which was removed when applying criterion 4 (see Figure 3).

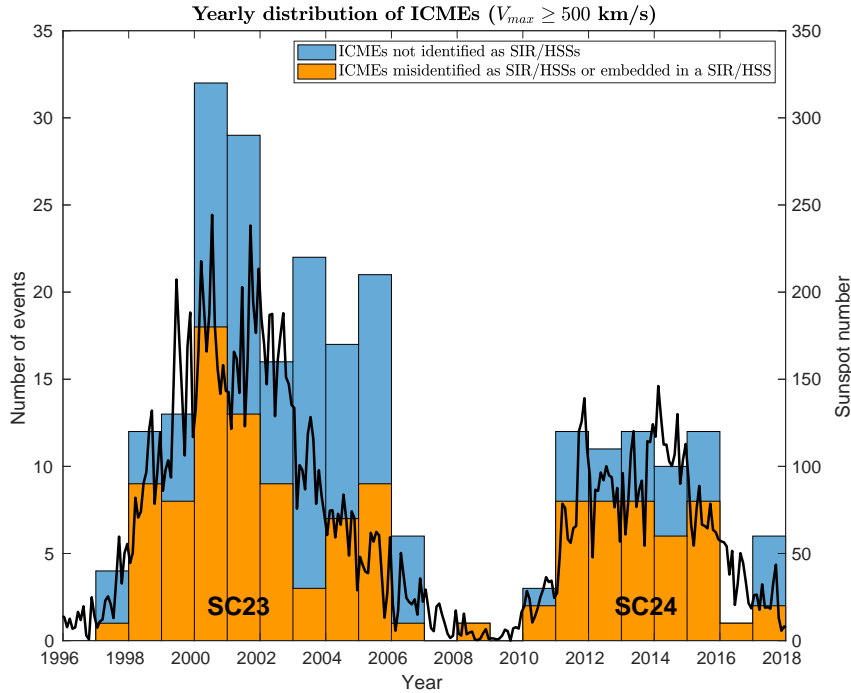


Figure 3. Histogram, left axis: Yearly distribution of ICMEs from *Richardson and Cane* [2010] (updated online version of January 2019) with $V_{\max} \geq 500$ km/s during 1996–2017 (envelope) and, among these, ICMEs misidentified as SIR/HSSs by the algorithm or ICMEs embedded in a SIR/HSS (orange). Black line, right axis: Monthly sunspot number during those years.

during ICMEs quite often exhibit similar features as SIR/HSSs. This issue is not severe during solar minimum years, but becomes important during solar maximum years. One must also keep in mind that some of the rejected events may be real SIR/HSS events that are interacting with a simultaneously occurring ICME event near the ecliptic plane [see, e.g., *Al-Shakarchi and Morgan*, 2018; *Shugay et al.*, 2018].

4 Results

4.1 Overall Features of Detected Events

In order to provide an overview of all the detected events during 1995–2017, Figure 4 displays the solar wind velocity plotted as a function of year (y -axis) and day of solar rotation (x -axis), when using Bartels rotations (27-day period). The time series starts from 1 January 1995 on day 17 of Bartels rotation 2204 and follows the horizontal axis until day 27, and then continues above from day 0 of Bartels rotation 2205 which starts on 11 January, and so on. The y -axis however indicates year instead of Bartels rotation number for an easier comparison with the other figures. This way of displaying the solar wind speed enables one to identify features recurring over several solar rotations, which appear as vertical structures in the plot. Two horizontal magenta dashed lines, in August 1996 and December 2008, indicate the transitions between solar cycles 22 and 23, and solar cycles 23 and 24, respectively, obtained from ftp://ftp.ngdc.noaa.gov/STP/space-weather/solar-data/solar-indices/sunspot-numbers/cycle-data/table_cycle_dates_maximum-minimum.txt. The starting dates of the detected SIR/HSS events are indicated as white filled circles on top of the solar wind velocity color plot. Several features indicating recurring elevated solar wind velocities can be identified, in particular during year 1995,

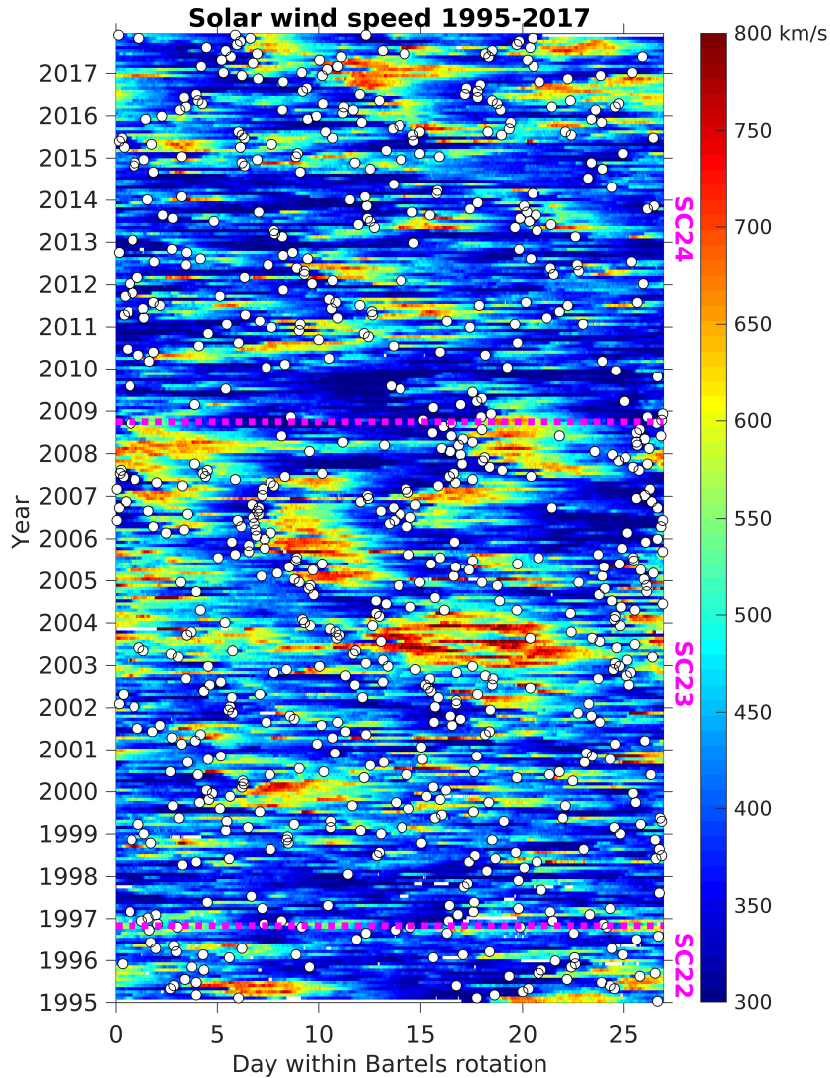


Figure 4. Color plot: Solar wind velocity plotted as a function of day number within 27-day Bartels rotation (x -axis, 1 Jan 1995 corresponds to day 17 of Bartels rotation 2204) and year from 1995 to 2017 (y -axis). White circles: starting dates of the detected SIR/HSS leading edges. The magenta dashed lines indicate the boundaries between solar cycles obtained from ftp://ftp.ngdc.noaa.gov/STP/space-weather/solar-data/solar-indices/sunspot-numbers/cycle-data/table_cycle-dates_maximum-minimum.txt.

years 2003–2004, years 2003–2008, and from 2015 onwards. During one solar rotation period, there may be several recurring intervals of high-speed flows. Discussion of the origin of these long-lived recurring high-speed streams is beyond the scope of the present paper, but one can note that, e.g., *Temmer et al.* [2007] suggest that the 9-day period in solar wind parameters, showing up as higher harmonic of the solar rotation frequency, is caused by the “periodic” longitudinal distribution of coronal holes on the Sun recurring for several solar rotations, especially during January–September 2005. This 9-day periodicity can be seen in Figure 4 during that time period, with enhanced solar wind speed recurring around Bartels rotation day 0, day 9, and day 18. It is noteworthy that structures from which high-speed solar wind flows may remain present at a same phase of the Bartels rotation for up to several years (see, e.g., the high-velocity signatures near the longitude corresponding to day 10, recurring from early 2005 until late 2006, or those near the longitude corresponding to day 2, recurring from mid 2006 until late 2008). This is consistent with findings by *Heidrich-Meisner et al.* [2017] who studied a same coronal hole structure for twelve solar rotations in 2006. The resulting HSS reached the Earth eleven times, yet exhibiting variability in its signature observed by ACE at L1 as the spacecraft mapping drifted to different regions within the coronal hole. On the other hand, *Krista et al.* [2018] tracked equatorial coronal holes at the surface of the Sun during 2011–2014 using the unique 360° coverage offered by the configuration of the Solar–Terrestrial Relations Observatory (STEREO) constellation and the Solar Dynamics Observatory (SDO). During those years in the maximum phase of SC24, most equatorial coronal holes had a lifetime of less than 100 days (<4 solar rotations), which is consistent with the significantly smaller number of recurring HSSs observed at L1 during 2011–2014 compared to 2006, as can be seen in Figure 4.

During the declining phases of these solar cycles, the detected SIR/HSS events appear to be often recurring. During the rising phase of solar cycles 23 and 24, recurring HSS signatures are less prominent, and the detected events tend to occur at more random solar longitudes. This is in agreement with findings by *Borovsky and Denton* [2006] for the end of SC22 and the beginning of SC23. The fading of the recurring coronal hole signatures coincides quite strikingly with the transition between solar cycles 23 and 24 in late 2008, after which HSSs become less frequent for a couple of years.

Figure 5 shows the yearly number of SIR/HSS events with $V_{\max} \geq 500$ km/s detected by our method as a histogram plot, where all the events that are contaminated by ICMEs have been removed. The sunspot number is shown as a colored curve, which corresponds to four phases of solar cycles which we will consider below (in particular in section 4.2): rising phase (red), maximum (green), early declining phase (blue), and late declining phase (black). The selected time limits for the phases are given in Table 1. The criterion used to separate the rising, maximum and declining phases was that, for both cycles 23 and 24, the double peak of the monthly sunspot number be included in the maximum phase. The motivation for subdividing the declining phase of solar cycles into early and late parts was to obtain solar cycle divisions of roughly similar durations, and to reveal potential differences within the declining phase itself.

While it is well-known that high-speed streams are frequent during the declining phases of solar cycles [e.g., *Gonzalez et al.*, 1999], many events are also detected during the other phases of solar cycles 23 and 24, which is consistent with reports by *Richardson and Cane* [2012b] during solar cycles 20 to 23. It is noteworthy that even the rising phases contain a large number of SIR/HSS events, corresponding to 69% and 48% of yearly numbers during the declining phases of SC23 (rising-phase years: 1997–1999; declining-phase years: 2003–2008) and SC24 (rising-phase years: 2009–2010; declining-phase years: 2015–2017), respectively. In fact, as was noted by *Echer et al.* [2013], SIR/HSS events were responsible for 30% of the moderate geomagnetic storms taking place during the rising phase of SC23.

The following common characteristics appear to repeat during the two observed cycles. After the sunspot minimum is reached, the number of SIR/HSS events is at minimum in the beginning of a new cycle both during cycles 23 (year 1997) and 24 (year 2009), which is

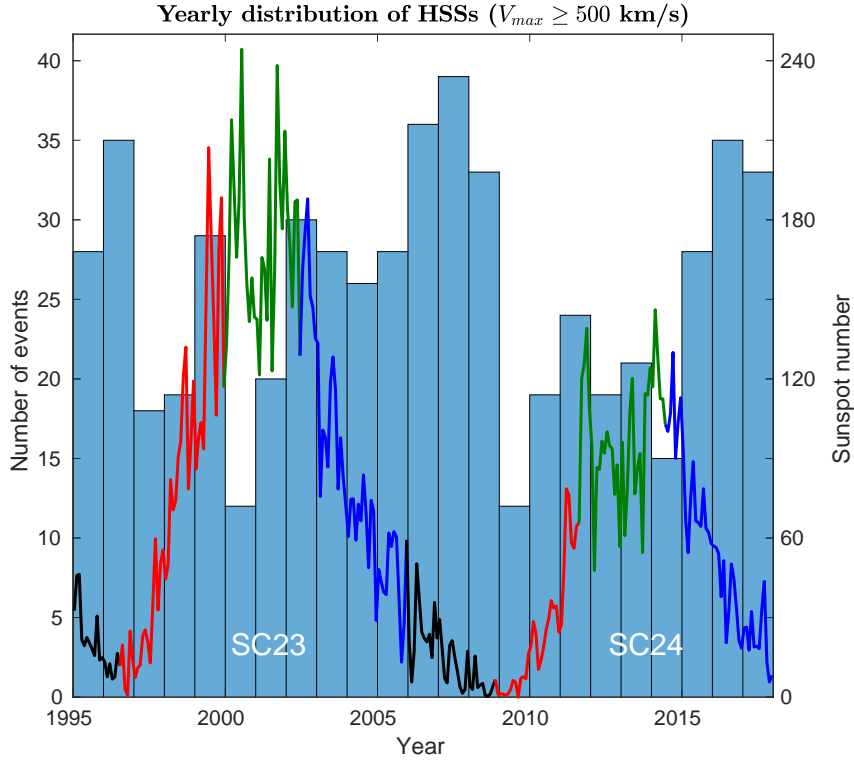


Figure 5. Histogram: Yearly distribution of high-speed stream events detected with the method using the criterion $V_{\max} \geq 500$ km/s. Line plot: Monthly sunspot number. The colors of the curve indicate the time intervals which are referred to as “rising phase” (red), “maximum” (green), “early declining phase” (blue) and “late declining phase” (black) of solar cycles.

Table 1. Subdivision of solar cycles (SC) between 1995 and 2017

Phase	Start date	End date	Duration (months)
SC 22 – late declining	Jan 1995	Jul 1996	19
SC 23 – rising	Aug 1996	Dec 1999	41
SC 23 – maximum	Jan 2000	Jun 2002	30
SC 23 – early declining	Jul 2002	Dec 2005	42
SC 23 – late declining	Jan 2006	Nov 2008	35
SC 24 – rising	Dec 2008	Aug 2011	33
SC 24 – maximum	Sep 2011	Jun 2014	34
SC 24 – early declining	Jul 2014	Dec 2017	42

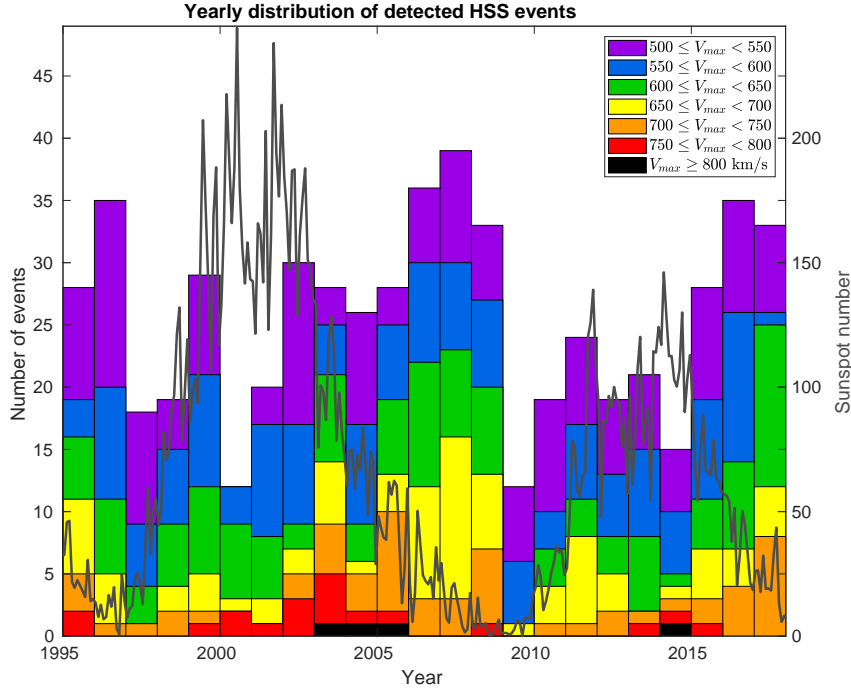


Figure 6. Histogram: Yearly distribution of high-speed stream events detected with the method and binned according to their maximum solar wind speed value. Line plot: Monthly sunspot number.

consistent with findings reported by *Jian et al.* [2011]. Then the number of SIR/HSSs starts to increase during the next two years in the rising phase. During sunspot maximum years the increase stops and there is a local minimum (year 2000 for cycle 23 and year 2014 for cycle 24). Even if one added the HSSs rejected because they contain an embedded ICME (part of the orange bars in Figure 3), the number of SIR/HSS events would still drop and a local minimum would still be found during these years (2000 and 2014). This confirms the observation made by *Jian et al.* [2006] during the maximum phase of solar cycle 23.

In the early declining phase of solar cycles, the number of SIR/HSS events starts to increase again and the maximum number of events occurs obviously during the last year of cycle 22 (1996, but we have data only for the last two years) and the second last year (2007) for cycle 23. For cycle 24, the number of events has almost the same values for the last two observed years, i.e., 2016 and 2017. If the length of cycle 24 were the nominal 11 years, this would imply that sunspot minimum would take place in 2019 and we could expect to have the maximum number of SIR/HSS events in year 2018 or 2019. The number of SIR/HSS events in 2007 is 39, and there were 35 events in years 1996 and 2016. These numbers correspond roughly to 3 SIR/HSS events per month with maximum speeds exceeding 500 km/s during maximum occurrence.

One interesting characteristic of the detected SIR/HSS events is the distribution of their maximum solar wind speed. Figure 6 gives the yearly distribution of the 588 detected SIR/HSS events, binned according to their maximum solar wind speed value during the first three days in the 1 h resolution data. The following clear features can be observed. First, during the first full year of a new cycle, when the number of SIR/HSS events is very low, the velocities of the HSSs are also low (years 1997 and 2009) with maximum velocities remaining mainly below 600 km/s. Second, during the declining phases, when the number of SIR/HSS event maximizes, the proportion of events with velocities higher than 650 km/s also increases. Third, HSS velocities larger than 750 km/s are very rare and occur typically

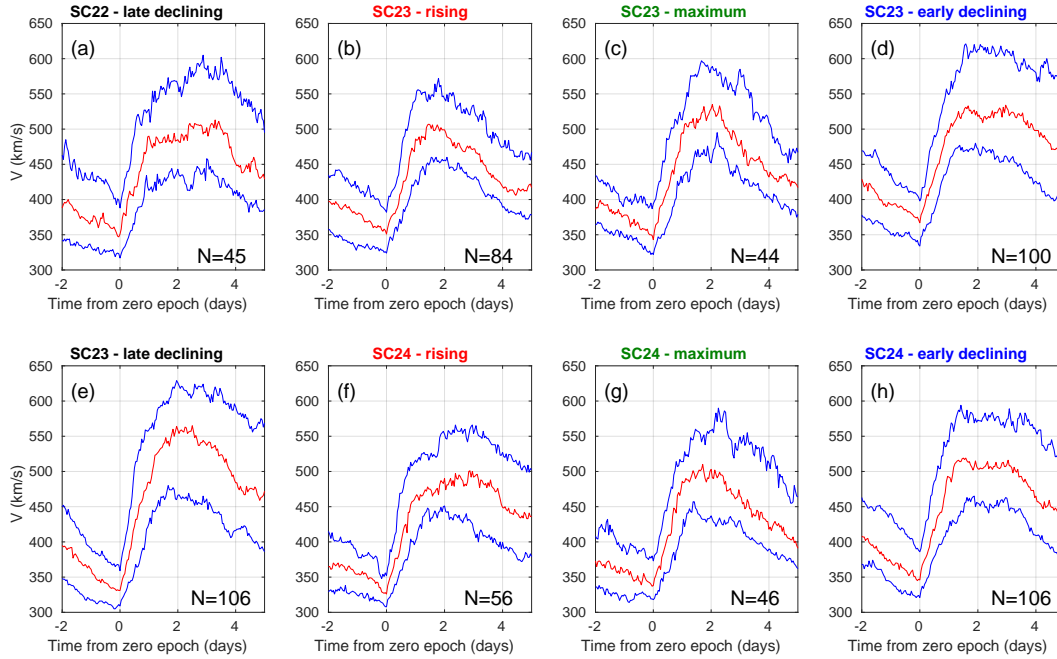


Figure 7. Superposed epoch analysis of the solar wind speed during SIR/HSS events during (a) the late declining phase of SC22, (b) the rising phase of SC23, (c) the maximum of SC 23, (d) the early declining phase of SC23, (e) the late declining phase of SC23, (f) the rising phase of SC24, (g) the maximum of SC24, and (h) the early declining phase of SC24. The number indicated in the bottom-right-hand corner of each panel corresponds to the number of SIR/HSS events during the corresponding solar cycle subdivision (cf. Figure 5).

0-2 times per year. Year 2003 is an exception with five events having maximum velocities exceeding 750 km/s (starting on 26 July, 5 August, 19 August, 16 September, 7 December).

4.2 SIR/HSS Event Evolution as a Function of Solar Cycle Phases

A comparison of SIR/HSS features during the solar cycle phases defined in Figure 5 is made using the superposed epoch analysis method, which was used in *Grandin et al.* [2015, 2017]. The superposed epoch method is a statistical analysis invented by *Chree* [1913], based on the collection of a large number of events, the definition of a reference time called “zero epoch” in the event timeline and the extraction of statistical properties (e.g., mean, median, and standard deviation) of the physical parameters of the events as a function of time relative to the zero epoch [see also 3.1 in *Grandin*, 2017]. Figures 7 to 12 show the statistical behaviors of key solar wind parameters and geomagnetic indices during high-speed stream events taking place at each solar cycle phase.

Figure 7 shows the superposed epoch analysis of the solar wind velocity during the SIR/HSS events detected during (a) the late declining phase of SC22, the (b) rising, (c) maximum, (d) early declining and (e) late declining phases of SC23, and the (f) rising, (g) maximum and (h) early declining phases of SC24. In each panel, median values are shown in red, and upper and lower quartiles in blue. The data are plotted from two days before the zero epoch until five days after, the zero epoch of each event corresponding to its starting time given by the algorithm. The number of events used to obtain the curves in each panel is given in the bottom-right-hand corner of the panel.

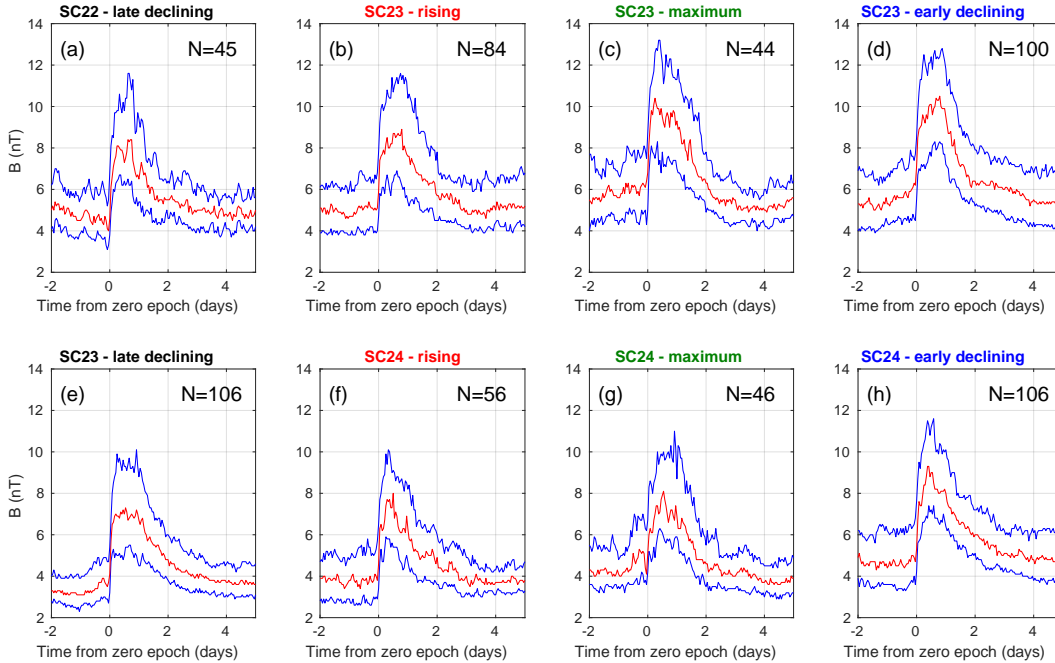


Figure 8. Same as Figure 7 for the IMF magnitude.

Out of these eight panels, the highest median velocities take place during the late declining phase of SC23 covering years 2006–2008 (panel e). The maximum median velocity in these superposed epoch plots reaches values of ≥ 550 m/s from the end of day 2 to the beginning of day 3 (please note that values 0–1 in the x axis correspond to day 1 and values from 1 to 2 to day 2). Second largest velocities are found in the early declining phases of SC23 and SC24 (panels d and h). Clearly smallest velocities occur in the rising phases of solar cycles (panels b and f).

It looks a bit surprising that the velocity in the late declining phase of SC22 is not showing particularly high values, unlike in SC23. The answer may be related to the special characteristics of the long-lasting solar minimum at the end of SC23. The study of coronal holes by *de Toma* [2011] provides insight in this topic. According to *de Toma* [2011], during the 1996 solar minimum, the two large polar coronal holes were the dominant coronal holes on the Sun and stable sources of fast solar wind over the poles, like in typical solar minimum conditions. This gave a relatively slow solar wind at the Earth, originating mostly from the edges of the polar coronal holes. However, the long period of low solar activity from 2006 to 2009 was characterized by weak polar magnetic fields and polar coronal holes smaller than observed during the previous minimum. Instead, large low-latitude coronal holes were present on the Sun until 2008 and remained important sources of recurrent high-speed solar wind streams. By early 2009, most the low-latitude coronal holes had closed down. With the increase of the new SC24 activity, small, mid-latitude coronal holes appeared. The fast wind in the rising phase was coming mostly from the edges of the polar coronal holes and occasionally from the small, mid-latitude coronal holes. Finally, the high-speed wind in the declining phases comes typically from the low-latitude coronal holes [*de Toma*, 2011].

Figure 8 shows the IMF magnitude B in the same format. The largest values for B in the SIR are found in the early declining and maximum phases of SC23 with the median values exceeding 10 nT during day 1. Inside SC24, the largest values of B take place in the early declining phase with median values reaching 9 nT. This is a confirmation that the maximum B value in SIRs does not simply follow solar activity given by the monthly sunspot number,

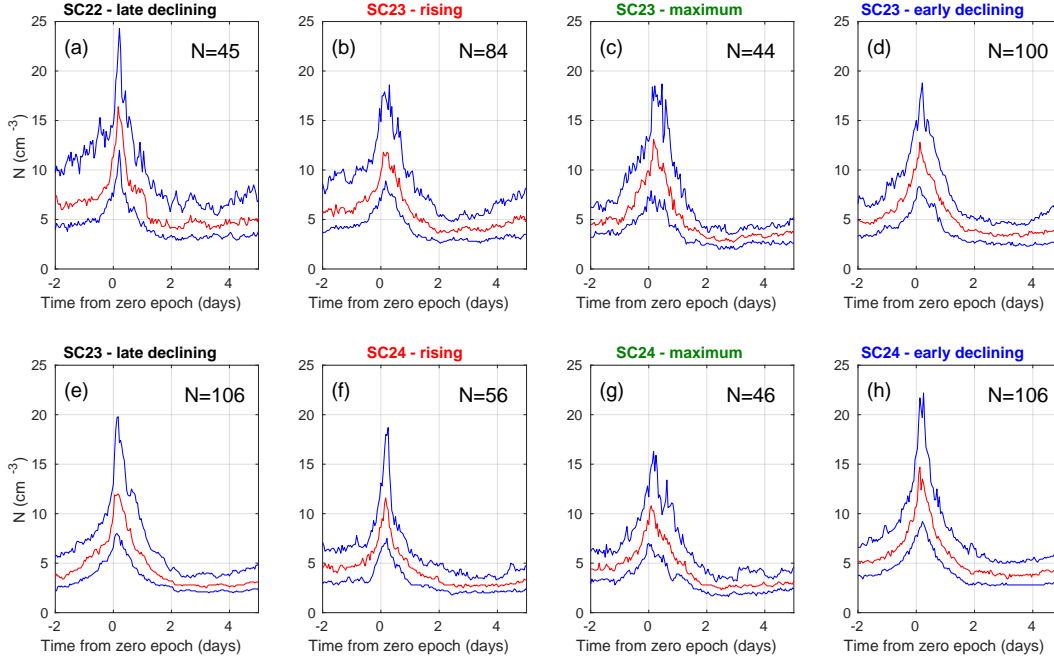


Figure 9. Same as Figure 7 for the solar wind density.

as was observed by *Jian et al.* [2006] when studying SC23. The lowest values are observed in the late declining phase of SC23, when the peak values of the median curve just reach 7 nT. These values are clearly smaller than in the late declining phase of the previous cycle, SC22. However, the difference comes mainly from the fact that the magnetic field values prior to the arrival of the SIR are clearly smaller in SC23, namely about 3 nT on day -1 , whereas in SC22 the corresponding value is about 4.5 nT. The low values of B at 1 AU near the ecliptic plane during the 2007–2008 solar minimum period of SC23 have been a topic of many studies [see, e.g., *Lee et al.*, 2009; *Wu et al.*, 2013].

When comparing SC23 and SC24, a clear overall difference can be found. It appears that the SC23 data (panels b, c, and d) have their peaks of median B 15–20% higher than the corresponding SC24 data (panels f, g, and h).

Figure 9 shows the superposed epoch analysis of the solar wind number density. The density has a narrow peak very shortly after the zero epoch for each solar cycle phase. The largest median values are obtained in the late declining phase of SC22 and the early declining phase of SC24, in both cases with values close to 15 cm^{-3} . Again, the late declining phase of SC23 is anomalous, since the background densities before the arrival of SIRs are only about 3.5 cm^{-3} in SC23, while in SC22 the values are about 6 cm^{-3} . In the region of high speeds, the solar wind is dilute, and the densities are about 2.5 cm^{-3} in SC23, while in SC22 the densities are about 4 cm^{-3} . *Lee et al.* [2009] noticed that when all solar wind OMNI data are considered, the peak occurrence for SC22 is centered at 3.5 cm^{-3} and for SC23 at 2.5 cm^{-3} . Obviously the rarefaction regions of HSSs dominate in the overall OMNI data.

Figure 10 shows the superposed epoch analysis of Akasofu ε (expressed in GWh), which has been calculated by using equation (1). Since the ε parameter depends linearly on solar wind velocity V and on the quadratic value of B , we expect that the cycle phases where these parameters maximize will have the largest values for ε . In addition, there is a strong dependence on the IMF clock angle, which is not shown in the previous plots. However, across several tens of events, the clock angle can be expected to take very different values, as the IMF will be northward in some events, southward in others, and with $B_z \approx 0$ in yet

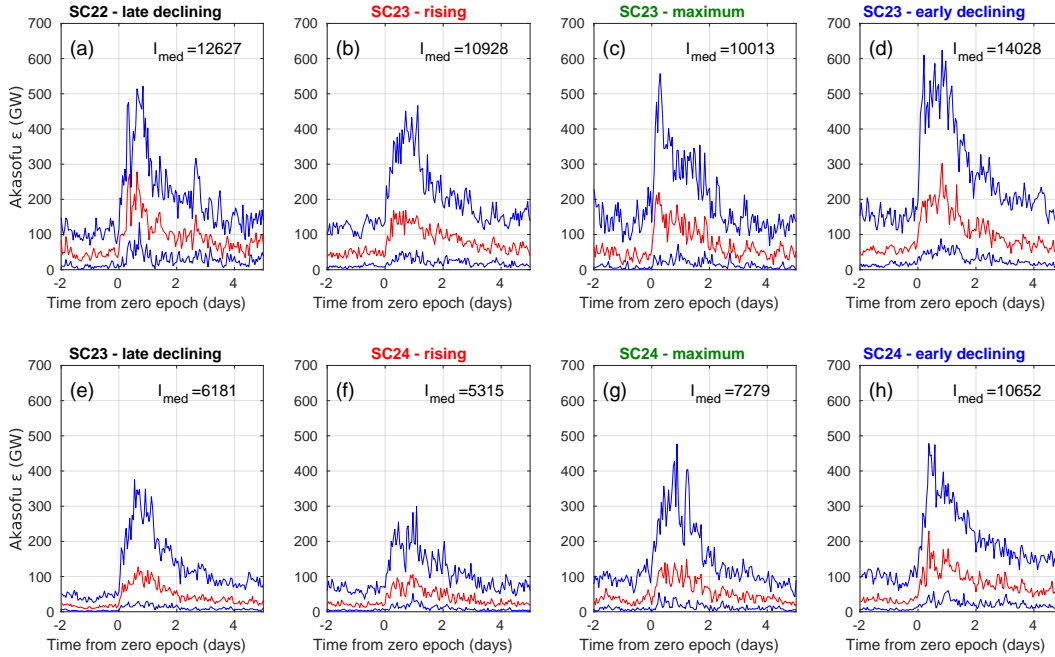


Figure 10. Same as Figure 7 for the Akasofu ε parameter, except that the number given in the top-right-hand corner of each panel corresponds to the integrated value of the median curve from the zero epoch until day 5 (in GWh).

some other events. Therefore, one may expect that, in the superposed epoch analysis, the effect of the clock angle on the value of Akasofu ε is averaged out. It can be seen that the highest individual median value of the ε parameter takes place in the early declining phase of SC23, where B has the largest values and V is relatively large. Almost as large values are seen in the late declining phase of SC22, which may be explained by the fact that the solar wind speed reached high values while B was still peaking.

In order to assess the sustained impact of the SIR/HSSs on the geospace environment, the median values of the Akasofu ε parameter were also integrated from the zero epoch until day 5, and those values are given in the panels of Figure 10 as I_{med} . The early declining phase of SC23 shows the largest integrated value of Akasofu ε . It also has the largest upper quartile values. The second highest integrated value is in the late declining phase of SC22, and the third highest value in the early declining phase of SC24. Even though the late declining phase of SC23 had the largest velocities, the Akasofu ε parameter has low values, due to the low values of B during the extended solar minimum, as discussed above. These are the second lowest values of all the studied phases. The lowest values are found in the rising phase of SC24.

Overall, Akasofu ε remains significantly lower during SC24 compared to SC23. In each phase, the energy input peaks around day 1 following the zero epoch, the value remains high until the end of day 2 and then decreases but remains somewhat elevated at least until day 5.

Figures 11 and 12 show the AE and $SYM-H$ indices, respectively. In general, the maximum of substorm (AE) and storm ($SYM-H$) activity is reached about one day after the zero epoch, in the beginning of day 2, which is before the solar wind speed reaches its maximum and hence corresponds to the stream interaction region rather than the HSS itself. *Burlaga and Lepping [1977]* showed that SIRs often amplify Alfvén waves propagating away from the Sun, which cause the IMF B_z component to alternate between northward and south-

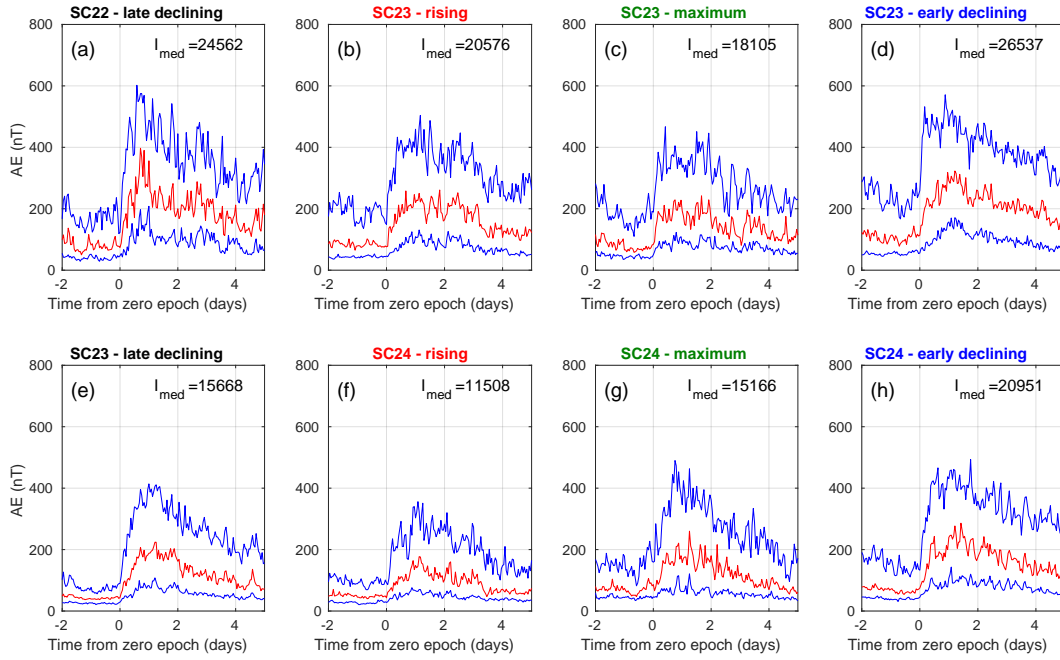


Figure 11. Same as Figure 10 for the AE index (integrated values in nTh).

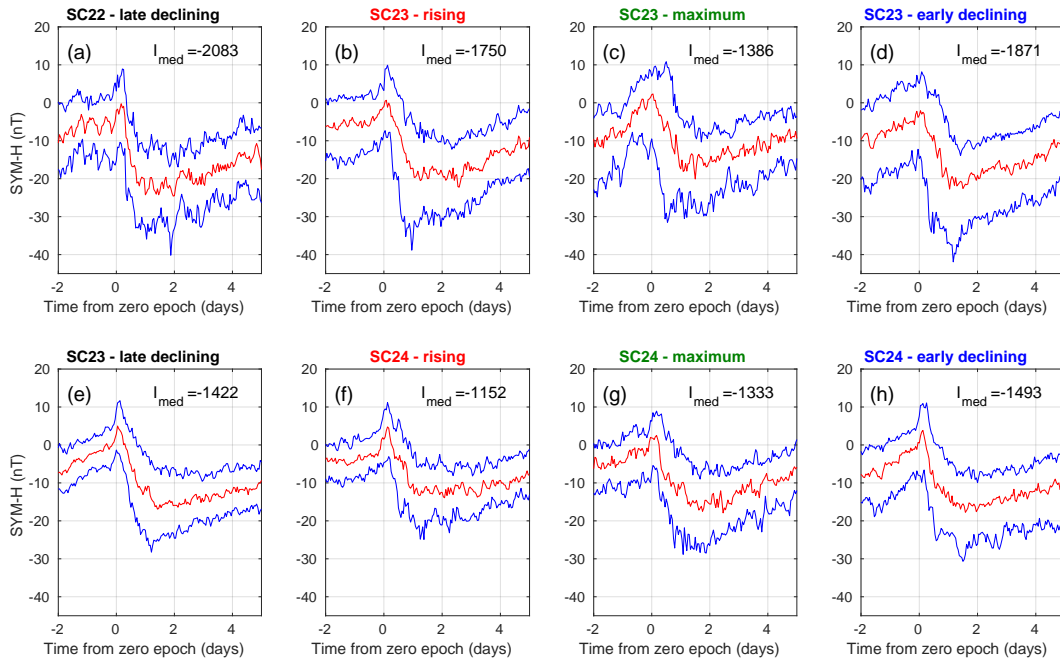


Figure 12. Same as Figure 10 for the SYM-H index (integrated values in nTh).

ward and therefore produce intermittent substorm activity while the SIR passes by Earth. Alfvén waves are also often present throughout the fast streams, which are also geoeffective. This is illustrated by the fact that the *AE* index remains enhanced at least until day 5. It is well-known that the geoeffectiveness of HSSs in terms of substorm activity is also largely controlled by the sign of B_z [e.g. *Kavanagh et al.*, 2012], which explains the rather large dispersion of the *AE* index values following the zero epoch indicated by the upper and lower quartile values in blue and the fairly broad *AE* peak.

Akasofu ε orders the *AE* index values quite well, so that the three most intense phases and the weakest one (rising phase of SC24) are the same for *AE* as for Akasofu ε . The same holds for *SYM-H*, except that the order of the two most intense events is reversed. Typically, the storms produced by SIR/HSSs are rather weak and only a few percent of the SIRs can produce intense geomagnetic storms ($Dst < -100$ nT) [*Richardson et al.*, 2006]. However, HSSs are quite effective in producing substorms, and these events are called HILDCAA (high-intensity long-duration auroral activity) by *Tsurutani et al.* [2006]. It was found by *Hajra et al.* [2013] that HILDCAAs are on average 20% longer during the declining phase than during the rising and maximum phases. Figure 11 shows indeed that during the declining phases the *AE* index is still elevated on day 5. In addition, the maximum *AE* values are higher during the early declining phases of SC23 and SC24 than during the other phases.

Again, the top-row panels of Figures 11 and 12 exhibit a more intense response than the bottom-row panels, underlining that geomagnetic activity related to SIR/HSSs significantly decreased between the early and late declining phases of SC23. Within a given solar cycle, the rising and maximum phases are those with lowest geomagnetic activity during SIR/HSS events, whereas the early and late declining phases exhibit stronger activity.

Figure 13 visualizes the 5-day integrated values of geomagnetic activity measured by *AE* (orange bars) and *SYM-H* (blue bars) during SIR/HSS events within the defined solar cycle phases from 1995 to 2017, superposed on the monthly sunspot number (black line). This figure shows the well-known importance of declining phases of the solar cycles for geomagnetic activity. For SC22, we have data only for the late declining phase, and it is the most geoeffective one in terms of *SYM-H*, and the second-most geoeffective in terms of *AE* for all data. Inside SC23, the early declining phase is the most geoeffective one in terms of both indices, and in terms of *AE* the most geoeffective one of all data. The anomalous late declining phase of SC23 is the least geoeffective one, and even the rising phase of this cycle is more geoeffective. The maximum phase is less geoeffective than the rising phase in SC23. When moving to SC24, the geoeffectiveness clearly decreases compared to SC23, as does the sunspot number. The early declining phase is the most geoeffective one inside SC24, but we do not yet have data for the late declining phase. Contrary to SC23, the maximum phase is more geoeffective than the rising phase. Comparing SC24 to SC23 in terms of auroral electrojet and substorm activity measured by the *AE* index, the geoeffectiveness has been about 40% lower in the rising phase, 15% lower in the maximum phase, and 20% lower in the early declining phase. For the ring current and storms measured by the *SYM-H* index, the geoeffectiveness has been about 35% lower in the rising phase and 20% lower in the early declining phase, but roughly similar during the maximum phase.

As a summary, we find that the geoeffectiveness of SIR/HSSs varies in the different phases of the solar cycle. Our results are in line with the often presented statement that SIR/HSSs are the most geoeffective during the declining phases of solar cycle [e.g., *Hajra et al.*, 2013; *Kilpua et al.*, 2017; *Chi et al.*, 2018], even though we find that the late declining phase of SC23 was very weakly geoeffective owing to reasons discussed in the next section.

5 Discussion

We will discuss two major topics. First, the validity of the detection algorithm is assessed by comparing the obtained list of SIR/HSS events with existing catalogs during years

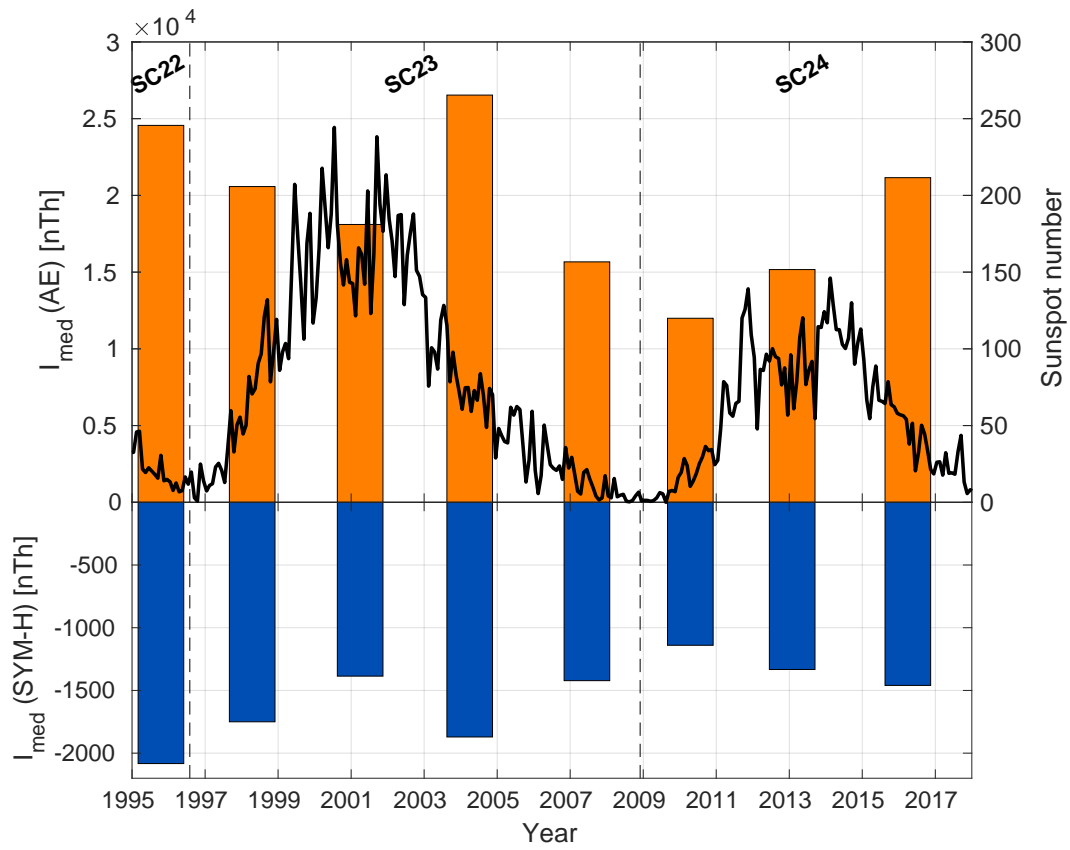


Figure 13. Bar diagram: Integrated values of median curves from the zero epoch until day 5 for the *AE* (top) and *SYM-H* (bottom) indices (see Figures 11 and 12). Line plot: Monthly sunspot number.

when they overlap. Second, the identified solar cycle phase-dependent features of SIR/HSSs and their geoeffectiveness will be considered in the global picture of the known features of the studied solar cycles.

5.1 Comparison with other HSS event lists

We compared the events detected by our algorithm with the HSS catalog issued by Mariş Muntean et al. (<http://www.geodin.ro/varsiti/>), which covers years from 2009 until 2016. We selected year 2015 for the comparison, as it is at the beginning of the declining phase of SC24 and hence contains a mix of HSSs, ICMEs and slow solar wind. The Mariş Muntean et al. catalog is solely based on the solar wind speed, averaged at 3 h resolution. A HSS event is detected if the maximum 3 h mean speed during one day exceeds the minimum 3 h mean speed of the previous day by at least 100 km/s, and if the enhanced speed persists for two days. In 2015, with their method, Mariş Muntean et al. detected 44 HSS events. Comparatively, our algorithm detected only 27 SIR/HSS events during that year. Two main reasons explain this first difference: (i) the Mariş Muntean et al. catalog does not focus on SIR-related HSSs, and hence contains 11 events corresponding to (or contaminated by) ICMEs (by comparison with the Richardson and Cane list), and (ii) the Mariş Muntean catalog is not restricted to HSSs with $V_{\max} \geq 500$ km/s, and therefore contains another 10 events whose maximum velocities lie between 400 and 500 km/s. On the other hand, our algorithm detected four SIR/HSS events which are not in the Mariş Muntean et al. catalog (on 14 July, 18 August, 2 September, and 28 November 2015). Figure S1 in Supporting Information illustrates the comparison of the two lists for 2015. For the 23 events common to both catalogs, 16 of them have their starting time with less than 6 h difference, and only one of them has starting time differing by more than 12 hours (2 January, 23 UT vs 4 January, 9–12 UT). For this specific event, our starting date nicely corresponds to the solar wind density peak, which makes this detection time consistent with the rest of the list (see Figure 9).

Another HSS catalog was earlier compiled by *Gupta and Badruddin* [2010] for years 1996–2007. The retained criteria are essentially the same as those used by Mariş Muntean et al., i.e., an increase in the solar wind speed of at least 100 km/s with sustained velocity for at least two days. Year 1996 was chosen for comparison of our list with the *Gupta and Badruddin* [2010] catalog, since it corresponds to the peak of SIR/HSS activity at the transition between SC22 and SC23. *Gupta and Badruddin* [2010] listed 40 HSS events in 1996, but several of them actually contained two to three distinct streams, therefore representing at total of 58 individual streams (compared to 35 events from our method). Among these, 22 events were associated with solar wind speeds remaining below our threshold of 500 km/s. One of their events (19 September) was not detected by our algorithm, since its initial solar wind speed was greater than 450 km/s (see criterion 2a), and another one (the second stream of the event starting on 8 April) was also rejected for being too soon after our 11 April event (see criterion 3). On the other hand, our algorithm detected a SIR/HSS event on 2 July, which is not included in the *Gupta and Badruddin* [2010] catalog. Besides these few differences, there is an overall good agreement between both catalogs. Figure S2 in Supporting Information illustrates the comparison of the two lists for 1996.

A third list of HSSs which may be used for comparison is the one given in *Morley et al.* [2010], which uses different criteria for SIR/HSS identification. As a first criterion, *Morley et al.* [2010] looked for an enhancement in the radial velocity of the solar wind (V_x) associated with a west–east deflection of the flow, i.e., a change in the sign of V_y . For the obtained SIR/HSS candidates, other solar wind parameters such as the IMF magnitude, the proton number density and the proton temperature were then examined to reject false positives. In addition, two consecutive events had to be separated by at least 2 days, and events exhibiting clear ICME signatures were removed from the list. The list given in Table 2 of *Morley et al.* [2010] considers 67 stream interfaces verifying those criteria between 2005 and 2008. During these same years, our algorithm detected 136 SIR/HSS events, which is more than twice as many. Yet, of the 67 events studied by *Morley et al.* [2010], we found that nine

of them were not detected by our algorithm. In two of these cases, a ICME was reported in the Richardson and Cane list (criterion 4), in three cases, the maximum solar wind speed did not reach 500 km/s (criterion 2c), and in four cases a previous event was detected less than three days before the rejected event (criterion 3). Figures S3–S6 in Supporting Information illustrate the comparison of the two lists for 2005–2008.

For the 58 SIR/HSS events in common with the *Morley et al.* [2010] list, a comparison of the starting times reveals that in all cases but one our algorithm gives an earlier time. This is inherent to the difference in the criteria for setting the beginning of the events: while our algorithm retains the time after which the solar wind speed starts increasing, *Morley et al.* [2010] were interested in the stream interface itself, which is determined with the azimuthal flow reversal (V_y sign change). The difference Δt_0 between those starting times can vary significantly. Figure S7 in Supporting Information gives a histogram of Δt_0 , which is defined as positive when our algorithm gives an earlier time than in the *Morley et al.* [2010] list. The peak in the distribution of Δt_0 is for values comprised between 6 and 12 hours, but up to 70 hour difference was found for a couple of events. The first such event (3 May 2006) exhibits steady solar wind speed enhancement for three days before the stream interface, and in the second case (7 February 2008), our method detects a small stream immediately preceding the main event, hence causing an erroneously early starting time. The difference is negative in only one case (22 April 2008), for which the start time given by our algorithm corresponds nicely to the beginning of the solar wind speed increase.

Finally, the list obtained with the detection method presented in this paper can be compared to the catalog compiled by *Jian et al.* [2006], later extended to cover years 1995 to 2009 (extended version available at http://www-ssc.igpp.ucla.edu/~jlan/ACE/Level3/SIR_List_from_Lan_Jian.pdf). Between 1995 and 2009, the *Jian et al.* [2006] list contains 437 SIR/HSSs with $V_{\max} \geq 500$ km/s, whereas our list contains 394 events during the same time 15-year period. When making a detailed analysis of the differences between those two lists, it appears that 39 events from our list are not present in the *Jian et al.* list. These events have each been examined visually to ensure they do exhibit typical SIR/HSS signatures. The reason for the difference may be that the event identification by *Jian et al.* [2006] imposes that the events must exhibit at least five out of the seven expected features considered in their study, which are solar wind speed increase, total perpendicular pressure pileup, velocity deflections, proton density enhancement, proton temperature enhancement, increase in entropy, and magnetic field compression. On the other hand, 82 events with $V_{\max} \geq 500$ km/s in the *Jian et al.* list are not present in ours. The reasons are: presence of an ICME with $V_{\max} \geq 500$ km/s within $[t_0 - 1 \text{ day}, t_0 + 3 \text{ days}]$ (32 events); $V_{\max} < 500$ km/s in the hourly OMNI data whereas the Wind or ACE data with 93 s and 64 s resolution, respectively, used by *Jian et al.* exceeds 500 km/s during the event (25 events); solar wind speed greater than 450 km/s at the start time of the event (15 events); compound events separated by less than 3 days (9 events); no sharp IMF magnitude gradient (1 event). Besides, in 27 cases, event starting dates differed by more than 24 h from one list to the other. About half of these cases correspond to compound events for which in one list the first event only is mentioned, while in the other list the second event only is mentioned. In the other cases, our list gives an earlier time than the *Jian et al.* list because the detected IMF magnitude enhancement is earlier than the leading edge of the SIR as identified by *Jian et al.* Overall, the agreement between both lists over those 15 years of comparison is satisfactory, and all the differences can be explained by the choices made in the criteria for identification in this study versus the *Jian et al.* study.

While some differences may be noted with each of those above-discussed catalogs, one advantage of the list obtained with this algorithm is that it contains SIR/HSS events during 23 years, i.e., roughly two solar cycles. Provided an updated list of ICMEs reaching the Earth exists and solar wind observations remain available, this list of SIR/HSS events can be completed during the upcoming years by applying the same algorithm, thus enabling further studies about the upcoming solar cycles.

5.2 Solar cycle variability of SIR/HSSs and geoeffectiveness

We have briefly discussed in the previous sections the properties of the solar wind at 1 AU near the ecliptic plane during the extended solar minimum of SC23 observed in other studies. Comparing the minimum periods of SC22 and SC23, *Lee et al.* [2009] noticed the following. For the IMF magnitude, the peak of the distribution for the SC23 period is centered at 3.5 nT, which is 30% less than 5 nT, the approximate central value for the peak of the SC22 distribution. For the number density, the distribution is shifted toward lower values by about 30%. For solar wind velocity, both the SC22 and SC23 velocity distributions have peak values occurring around 340 km/s, but for SC23 the peak is lower and the high-speed tail distribution, which is centered near 580 km/s, has slightly larger percent occurrence during SC23.

In this study, we have specifically studied the SIR/HSS events and our findings are in general accordance with *Lee et al.* [2009], but give some additional insight into the distribution functions. We found by comparing the late declining phases of SC22 and SC23, namely years 1995–1996 and 2006–2008, the following properties. Both the IMF magnitude and density values before the SIR/HSS events are about 30% lower in SC23 than SC22, but the compressions of B and N are equally strong in both cycles. The peak of the density distribution in *Lee et al.* [2009] study comes obviously from the dilute solar wind in the high-speed stream region (in our figures superposed epoch after day 2).

Comparison of the distributions of HSS peak velocities during the late declining phases of SC22 and SC23 shown in Figure 6 indicates that the proportion of $500 < V_{max} < 600$ km/s is higher in SC22, whereas the proportion of $V_{max} > 700$ km/s is higher in SC23. The superposed epoch presentation of velocities shown in Figure 7 confirms that the median peak velocities are higher in SC23 ($V_{max} \sim 560$ km/s) than SC22 ($V_{max} \sim 510$ km/s). These are in harmony with the observations of the behavior of the high-speed tail distributions by *Lee et al.* [2009].

The solar wind parameters control the coupling of the IMF with the terrestrial magnetosphere and energy transfer from the solar wind into the magnetosphere–ionosphere system. Several coupling functions have been developed [see, e.g., *Newell et al.*, 2007], which all depend on solar wind velocity and magnetic field. In this study, we have used the traditional Akasofu ε . We saw a very similar behavior between the Akasofu ε and the AE and $SYM-H$ indices. This can be expected, since it is well-known that the solar wind parameters directly affect the geoeffectiveness of SIR/HSSs. The surprisingly poor geoeffectiveness of the SIR/HSS events in the late declining phase of SC23 is obviously explained by the unusually low magnetic field values during the deep minimum of SC23 discussed above. Even though the velocities of these HSSs were higher than in the late declining phase of SC22, this did not make those more geoeffective, and this can be explained by the quadratic dependence on the magnetic field intensity compared to the linear dependence on the velocity in the coupling function. The fact that SIR/HSSs are less geoeffective during SC24 than during SC23 also finds an explanation in the solar wind properties. The velocities were a bit smaller during SC24 than SC23, but the magnetic fields were even more significantly smaller. This will be discussed more below.

Following the extremely low minimum of SC23, SC24 has shown unusually low activity [*Kamide and Kusano*, 2013]. In particular, *McComas et al.* [2013] showed that the rising phase of SC24 exhibited significantly lower key parameters (e.g., IMF magnitude, solar wind proton density, temperature, velocity, dynamic pressure) than the rising phases of previous solar cycles, which correlates with the fact that SC24 has been the weakest solar cycle since the beginning of the Space Age. Figures 7–12 indicate that this conclusion hold not only when looking at solar activity as a whole but also when focusing specifically on solar wind conditions during SIR/HSSs. It is noteworthy that, while the IMF magnitude (see Figure 8) had very low values during the late declining phase of SC23 as discussed above, the HSS peak velocity was meanwhile at its highest values, and started to drop only during the rising

phase of SC24 (see Figure 7) and remained at lower values than during the previous cycle. Even though the magnetic field has to some extent recovered from the deep minimum of SC23, it has continued to be at a lower level during SC24 than at the corresponding phases during SC23.

In fact, the early/late declining phase distinction for SC24 cannot presently be determined, as the minimum is still to be reached. Whether such a distinction will even be needed for SC24 is not certain, as it may be so that the unusually long declining phase of SC23 and the associated extremely weak activity conditions were unique.

6 Conclusions

We presented a method for detection of solar wind high-speed stream events, based on the IMF magnitude time derivative, the solar wind velocity, and, to remove ICMEs misidentified as SIR/HSSs and SIR/HSSs containing an embedded ICME, comparison with the Richardson and Cane list of ICMEs. This algorithm has been applied to years 1995–2017, leading to the detection of 588 SIR/HSS events with speeds exceeding 500 km/s. When compared to the existing HSS lists, which use slightly different criteria and may include a human visual detection of events, the algorithm proves efficient in correctly identifying SIR/HSS events and setting their beginning at the time when the solar wind speed starts increasing. The main benefit of this new detection method is that it produces a catalog of SIR/HSS events over 23 years of solar wind observations in a transparent and reproducible way.

The analysis of the 588 SIR/HSS events obtained with the detection method shows that the yearly number of SIR/HSS events peaks during the declining phase of the solar cycle. Besides the maximum yearly number of SIR/HSS events in SC23 (39 events in 2007) is about the same as the maximum number in 1995 of SC22 (35 events) and in 2016 of SC24 (35 events). It is yet to be seen if the yearly number of SIR/HSS events in SC24 increases when approaching the solar cycle minimum.

The number of SIR/HSS events sharply drops after the solar minimum is reached, during the first year of a new cycle. After that, the yearly number of events starts to rise. Even during the rising phases, which are associated with the smallest number of SIR/HSSs, the yearly number of SIR/HSSs amounts to 69% and 48% of the yearly number during the declining phases of SC23 and SC24, respectively. During the solar maximum years, which are dominated by ICME events, we find a local minimum in the occurrence of SIR/HSS events.

During the late declining phase of SC23, large low-latitude coronal holes persisted on the solar surface, which had long lifetimes. This resulted in repeated very-high-velocity streams. Even though the compressions of magnetic field were of the same magnitude as during the late declining phase of the previous SC22, the low background magnetic field values at 1 AU near the ecliptic plane during the extended minimum of 2007–2008 [consistent with results by *Lee et al.*, 2009; *Wu et al.*, 2013] resulted in low B values in the ecliptic SIR regions and in low solar wind coupling function (Akasofu ϵ) values. Hence, the geoeffectiveness of SIR/HSSs during the late declining phase of SC23 was the smallest of this entire cycle.

During SC24, both the solar wind velocity and the magnetic field have continued to be at a lower level than during the corresponding phases of SC23. Hence, the geoeffectiveness of SIR/HSSs has been lower too. For auroral electrojet and substorm activity measured by the AE index, the geoeffectiveness has been about 40% lower during the rising phase and 20% lower during the early declining phase. For the ring current and storms measured by the $SYM-H$ index, the geoeffectiveness has been about 35% lower during the rising phase and 20% lower during the early declining phase.

We can confirm the earlier-reported fact the SIR/HSS events have highest geoeffectiveness during the declining phases. However, there may be solar-cycle-dependent differences when one considers the early and late declining phases. The late declining phase of SC22 was very geoeffective, whereas the corresponding phase in SC23 was not. The early declining phase was the most geoeffective one inside SC23. So far, for SC24, the early declining phase has also been the most geoeffective one; however, we do not know yet how geoeffective SIR/HSSs will be during the late declining phase of SC24.

Acknowledgments

This work is supported by the Academy of Finland (projects 312351 and 285474) and the European Research Council (Consolidator Grant 682068-PRESTISSIMO). The OMNI data were obtained from the GSFC/SPDF OMNIWeb interface at <http://omniweb.gsfc.nasa.gov>. The monthly values of the sunspot number between 1995 and 2017 were retrieved from the World Data Center SILSO, Royal Observatory of Belgium, Brussels. The Richardson and Cane list of ICMEs was downloaded from <http://www.srl.caltech.edu/ACE/ASC/DATA/level3/icmetable2.htm>. The solar cycle beginning dates were determined from ftp://ftp.ngdc.noaa.gov/STP/space-weather/solar-data/solar-indices/sunspot-numbers/cycle-data/table_cycle-dates_maximum-minimum.txt. This work utilizes the HSS catalog issued by G. Mariş Muntean, D. Beşliu-Ionescu and V. Dobrică, managed by the Institute of Geodynamics of the Romanian Academy.

References

- Akasofu, S.-I. (1979), A search for the interplanetary quantity controlling the development of geomagnetic storms, *Royal Astronomical Society, Quarterly Journal*, *20*, 119–137.
- Al-Shakarchi, D. A., and H. Morgan (2018), Properties of the hps-icme-cir interaction event of 9–10 september 2011, *J. Geophys. Res. Space Physics*, *123*(4), 2535–2556, doi:10.1002/2017JA024849.
- Alves, M. V., E. Echer, and W. D. Gonzalez (2006), Geoeffectiveness of corotating interaction regions as measured by Dst index, *J. Geophys. Res. Space Physics*, *111*, A07S05, doi:10.1029/2005JA011379.
- Bame, S. J., J. R. Asbridge, W. C. Feldman, and J. T. Gosling (1976), Solar cycle evolution of high-speed solar wind streams., *The Astrophysical Journal*, *207*, 977–980, doi:10.1086/154566.
- Belcher, J. W., and J. Davis, Leverett (1971), Large-amplitude Alfvén waves in the interplanetary medium, *2, Journal of Geophysical Research*, *76*, 3534, doi:10.1029/JA076i016p03534.
- Borovsky, J. E., and M. H. Denton (2006), Differences between CME-driven storms and CIR-driven storms, *J. Geophys. Res. Space Physics*, *111*, A07S08, doi:10.1029/2005JA011447.
- Borovsky, J. E., and M. H. Denton (2009), Relativistic-electron dropouts and recovery: A superposed epoch study of the magnetosphere and the solar wind, *J. Geophys. Res. Space Physics*, *114*, A02201, doi:10.1029/2008JA013128.
- Burlaga, L. F., and R. P. Lepping (1977), The causes of recurrent geomagnetic storms, *Planetary and Space Science*, *25*, 1151–1160, doi:10.1016/0032-0633(77)90090-3.
- Chi, Y., C. Shen, B. Luo, Y. Wang, and M. Xu (2018), Geoeffectiveness of Stream Interaction Regions From 1995 to 2016, *Space Weather*, *16*, 1960–1971, doi:10.1029/2018SW001894.
- Chkhetia, A. M. (1975), Global distribution of the 27-day electron density variation at the maximum of the ionospheric F layer, *Geomagnetism and Aeronomy*, *15*, 160.
- Chree, C. (1913), Some phenomena of sunspots and of terrestrial magnetism at Kew Observatory, *Philosophical Transactions of the Royal Society of London Series A*, *212*, 75–116, doi:10.1098/rsta.1913.0003.

- Crowley, G., A. Reynolds, J. P. Thayer, J. Lei, L. J. Paxton, A. B. Christensen, Y. Zhang, R. R. Meier, and D. J. Strickland (2008), Periodic modulations in thermospheric composition by solar wind high speed streams, *Geophysical Research Letters*, *35*, L21106, doi:10.1029/2008GL035745.
- Davis, T. N., and M. Sugiura (1966), Auroral electrojet activity index AE and its universal time variations, *J. Geophys. Res.*, *71*, 785–801, doi:10.1029/JZ071i003p00785.
- de Toma, G. (2011), Evolution of coronal holes and implications for high-speed solar wind during the minimum between cycles 23 and 24, *Solar Physics*, *274*(1-2), 195–217.
- Denton, M. H., and J. E. Borovsky (2012), Magnetosphere response to high-speed solar wind streams: A comparison of weak and strong driving and the importance of extended periods of fast solar wind, *J. Geophys. Res. Space Physics*, *117*, A00L05, doi:10.1029/2011JA017124.
- Denton, M. H., T. Ulich, and E. Turunen (2009), Modification of midlatitude ionospheric parameters in the F2 layer by persistent high-speed solar wind streams, *Space Weather*, *7*, S04006, doi:10.1029/2008SW000443.
- Echer, E., B. T. Tsurutani, and W. D. Gonzalez (2013), Interplanetary origins of moderate ($-100 \text{ nT} < \text{Dst} \leq -50 \text{ nT}$) geomagnetic storms during solar cycle 23 (1996–2008), *J. Geophys. Res. Space Physics*, *118*(1), 385–392, doi:10.1029/2012JA018086.
- Gonzalez, W. D., B. T. Tsurutani, and A. L. Clúa de Gonzalez (1999), Interplanetary origin of geomagnetic storms, *Space Science Reviews*, *88*, 529–562, doi:10.1023/A:1005160129098.
- Gopalswamy, N., and M. Kundu (1992), Estimation of the mass of a coronal mass ejection from radio observations, *The Astrophysical Journal*, *390*, L37–L39.
- Gosling, J. T., and V. J. Pizzo (1999), Formation and Evolution of Corotating Interaction Regions and their Three Dimensional Structure, *Space Science Reviews*, *89*, 21–52, doi:10.1023/A:1005291711900.
- Gosling, J. T., A. J. Hundhausen, V. Pizzo, and J. R. Asbridge (1972), Compressions and rarefactions in the solar wind: Vela 3, *Journal of Geophysical Research*, *77*(28), 5442–5454, doi:10.1029/JA077i028p05442.
- Gosling, J. T., J. R. Asbridge, S. J. Bame, and W. C. Feldman (1976), Solar wind speed variations: 1962–1974, *J. Geophys. Res.*, *81*, 5061–5070, doi:10.1029/JA081i028p05061.
- Grandin, M. (2017), *Multi-instrument and modelling studies of the ionospheres at Earth and Mars*, (Doctoral dissertation). Retrieved from Jultika (<http://urn.fi/urn:isbn:9789526216157>). Sodankylä (Finland): University of Oulu.
- Grandin, M., A. T. Aikio, A. Kozlovsky, T. Ulich, and T. Raita (2015), Effects of solar wind high-speed streams on the high-latitude ionosphere: Superposed epoch study, *J. Geophys. Res. Space Physics*, *120*, 10,669–10,687, doi:10.1002/2015JA021785.
- Grandin, M., A. T. Aikio, A. Kozlovsky, T. Ulich, and T. Raita (2017), Cosmic radio noise absorption in the high-latitude ionosphere during solar wind high-speed streams, *J. Geophys. Res. Space Physics*, *122*, 5203–5223, doi:10.1002/2017JA023923.
- Gupta, V., and Badruddin (2010), High-Speed Solar Wind Streams during 1996–2007: Sources, Statistical Distribution, and Plasma/Field Properties, *Solar Physics*, *264*, 165–188, doi:10.1007/s11207-010-9554-z.
- Hajra, R., E. Echer, B. T. Tsurutani, and W. D. Gonzalez (2013), Solar cycle dependence of High-Intensity Long-Duration Continuous AE Activity (HILDCAA) events, relativistic electron predictors?, *Journal of Geophysical Research (Space Physics)*, *118*, 5626–5638, doi:10.1002/jgra.50530.
- Hapgood, M. A. (1993), A double solar cycle in the 27-day recurrence of geomagnetic activity, *Annales Geophysicae*, *11*, 248–253.
- Heidrich-Meisner, V., T. Peleikis, M. Kruse, L. Berger, and R. F. Wimmer-Schweingruber (2017), Evolution of an equatorial coronal hole structure and the released coronal hole wind stream: Carrington rotations 2039 to 2050, *Astronomy & Astrophysics*, *603*, A84, doi:10.1051/0004-6361/201730574.

- Iyemori, T. (1990), Storm-time magnetospheric currents inferred from mid-latitude geomagnetic field variations, *Journal of Geomagnetism and Geoelectricity*, *42*, 1249–1265.
- Jian, L., C. T. Russell, J. G. Luhmann, and R. M. Skoug (2006), Properties of Stream Interactions at One AU During 1995–2004, *Solar Physics*, *239*, 337–392, doi:10.1007/s11207-006-0132-3.
- Jian, L. K., C. T. Russell, and J. G. Luhmann (2011), Comparing Solar Minimum 23/24 with Historical Solar Wind Records at 1 AU, *Solar Physics*, *274*, 321–344, doi:10.1007/s11207-011-9737-2.
- Kamide, Y., and K. Kusano (2013), Is Something Wrong With the Present Solar Maximum?, *Space Weather*, *11*, 140–141, doi:10.1002/swe.20045.
- Kavanagh, A. J., F. Honary, E. F. Donovan, T. Ulich, and M. H. Denton (2012), Key features of >30 keV electron precipitation during high speed solar wind streams: A superposed epoch analysis, *J. Geophys. Res. Space Physics*, *117*, A00L09, doi:10.1029/2011JA017320.
- Kilpua, E. K. J., A. Balogh, R. von Steiger, and Y. D. Liu (2017), Geoeffective Properties of Solar Transients and Stream Interaction Regions, *Space Science Reviews*, *212*, 1271–1314, doi:10.1007/s11214-017-0411-3.
- King, J. H., and N. E. Papitashvili (2005), Solar wind spatial scales in and comparisons of hourly Wind and ACE plasma and magnetic field data, *J. Geophys. Res. Space Physics*, *110*, A02104, doi:10.1029/2004JA010649.
- Krieger, A. S., A. F. Timothy, and E. C. Roelof (1973), A Coronal Hole and Its Identification as the Source of a High Velocity Solar Wind Stream, *Solar Physics*, *29*, 505–525, doi:10.1007/BF00150828.
- Krista, L. D., S. W. McIntosh, and R. J. Leamon (2018), The Longitudinal Evolution of Equatorial Coronal Holes, *The Astronomical Journal*, *155*(4), 153.
- Lee, C., J. Luhmann, X. Zhao, Y. Liu, P. Riley, C. Arge, C. Russell, and I. de Pater (2009), Effects of the weak polar fields of solar cycle 23: Investigation using omni for the stereo mission period, *Solar physics*, *256*(1-2), 345–363.
- Lindsay, G. M., J. G. Luhmann, C. T. Russell, and J. T. Gosling (1999), Relationships between coronal mass ejection speeds from coronagraph images and interplanetary characteristics of associated interplanetary coronal mass ejections, *Journal of Geophysical Research*, *104*, 12,515–12,524, doi:10.1029/1999JA900051.
- Mathie, R. A., and I. R. Mann (2001), On the solar wind control of Pc5 ULF pulsation power at mid-latitudes: Implications for MeV electron acceleration in the outer radiation belt, *J. Geophys. Res.*, *106*, 29,783–29,796, doi:10.1029/2001JA000002.
- McComas, D. J., S. J. Bame, P. Barker, W. C. Feldman, J. L. Phillips, P. Riley, and J. W. Griffiee (1998), Solar Wind Electron Proton Alpha Monitor (SWEPAM) for the Advanced Composition Explorer, *Space Science Reviews*, *86*, 563–612, doi:10.1023/A:1005040232597.
- McComas, D. J., N. Angold, H. A. Elliott, G. Livadiotis, N. A. Schwadron, R. M. Skoug, and C. W. Smith (2013), Weakest solar wind of the space age and the current "mini" solar maximum, *The Astrophysical Journal*, *779*(1), 2.
- McPherron, R. L., and J. Weygand (2006), The Solar Wind and Geomagnetic Activity as a Function of Time Relative to Corotating Interaction Regions, in *Recurrent Magnetic Storms: Corotating Solar Wind*, vol. 167, p. 125, doi:10.1029/167GM12.
- Meredith, N. P., R. B. Horne, M. M. Lam, M. H. Denton, J. E. Borovsky, and J. C. Green (2011), Energetic electron precipitation during high-speed solar wind stream driven storms, *J. Geophys. Res. Space Physics*, *116*, A05223, doi:10.1029/2010JA016293.
- Morley, S., R. Friedel, E. Spanswick, G. Reeves, J. Steinberg, J. Koller, T. Cayton, and E. Noveroske (2010), Dropouts of the outer electron radiation belt in response to solar wind stream interfaces: global positioning system observations, *The Royal Society*, *466*(2123), 3329–3350, doi:10.1098/rspa.2010.0078.

- Neugebauer, M., D. Reisenfeld, and I. G. Richardson (2016), Comparison of algorithms for determination of solar wind regimes, *Journal of Geophysical Research (Space Physics)*, *121*, 8215–8227, doi:10.1002/2016JA023142.
- Newell, P. T., T. Sotirelis, K. Liou, C. I. Meng, and F. J. Rich (2007), A nearly universal solar wind-magnetosphere coupling function inferred from 10 magnetospheric state variables, *J. Geophys. Res. Space Physics*, *112*, A01206, doi:10.1029/2006JA012015.
- Ogilvie, K. W., D. J. Chornay, R. J. Fritzenreiter, F. Hunsaker, J. Keller, J. Lobell, G. Miller, J. D. Scudder, E. C. Sittler, Jr., R. B. Torbert, D. Bodet, G. Needell, A. J. Lazarus, J. T. Steinberg, J. H. Tappan, A. Mavretic, and E. Gergin (1995), SWE, A Comprehensive Plasma Instrument for the Wind Spacecraft, *Space Science Reviews*, *71*, 55–77, doi:10.1007/BF00751326.
- Reisenfeld, D. B., R. C. Wiens, B. L. Barraclough, J. T. Steinberg, M. Neugebauer, J. Raines, and T. H. Zurbuchen (2013), Solar Wind Conditions and Composition During the Genesis Mission as Measured by in situ Spacecraft, *Space Science Reviews*, *175*, 125–164, doi:10.1007/s11214-013-9960-2.
- Richardson, I. G. (2018), Solar wind stream interaction regions throughout the heliosphere, *Living Reviews in Solar Physics*, *15*, 1, doi:10.1007/s41116-017-0011-z.
- Richardson, I. G., and H. V. Cane (2010), Near-Earth Interplanetary Coronal Mass Ejections During Solar Cycle 23 (1996 - 2009): Catalog and Summary of Properties, *Solar Physics*, *264*, 189–237, doi:10.1007/s11207-010-9568-6.
- Richardson, I. G., and H. V. Cane (2012a), Solar wind drivers of geomagnetic storms during more than four solar cycles, *Journal of Space Weather and Space Climate*, *2*, A01, doi:10.1051/swsc/2012001.
- Richardson, I. G., and H. V. Cane (2012b), Near-earth solar wind flows and related geomagnetic activity during more than four solar cycles (1963-2011), *Journal of Space Weather and Space Climate*, *2*, A02, doi:10.1051/swsc/2012003.
- Richardson, I. G., E. W. Cliver, and H. V. Cane (2000), Sources of geomagnetic activity over the solar cycle: Relative importance of coronal mass ejections, high-speed streams, and slow solar wind, *J. Geophys. Res.*, *105*, 18,203–18,213, doi:10.1029/1999JA000400.
- Richardson, I. G., E. W. Cliver, and H. V. Cane (2001), Sources of geomagnetic storms for solar minimum and maximum conditions during 1972-2000, *Geophys. Res. Lett.*, *28*, 2569–2572, doi:10.1029/2001GL013052.
- Richardson, I. G., D. F. Webb, J. Zhang, D. B. Berdichevsky, D. A. Biesecker, J. C. Kasper, R. Kataoka, J. T. Steinberg, B. J. Thompson, C. C. Wu, and A. N. Zhukov (2006), Major geomagnetic storms ($Dst < -100$ nT) generated by corotating interaction regions, *J. Geophys. Res. Space Physics*, *111*, A07S09, doi:10.1029/2005JA011476.
- Richter, A. K., and A. H. Luttrell (1986), Superposed epoch analysis of corotating interaction regions at 0.3 and 1.0 au: A comparative study, *J. Geophys. Res. Space Physics*, *91*(A5), 5873–5878, doi:10.1029/JA091iA05p05873.
- Schwenn, R. (1983), Direct Correlations Between Coronal Transients and Interplanetary Disturbances, *Space Science Reviews*, *34*, 85–99, doi:10.1007/BF00221199.
- Sheeley, J., N. R., R. A. Howard, D. J. Michels, M. J. Koomen, R. Schwenn, K. H. Muehlhaeuser, and H. Rosenbauer (1985), Coronal mass ejections and interplanetary shocks, *Journal of Geophysical Research*, *90*, 163–176, doi:10.1029/JA090iA01p00163.
- Sheeley Jr, N., J. Harvey, and W. Feldman (1976), Coronal holes, solar wind streams, and recurrent geomagnetic disturbances: 1973–1976, *Solar Physics*, *49*(2), 271–278.
- Shugay, Y., V. Slemzin, D. Rodkin, Y. Yermolaev, and I. Veselovsky (2018), Influence of coronal mass ejections on parameters of high-speed solar wind: a case study, *Journal of Space Weather and Space Climate*, *8*, A28.
- SILSO World Data Center (1995-2017), The International Sunspot Number.
- Smith, C. W., J. L'Heureux, N. F. Ness, M. H. Acuña, L. F. Burlaga, and J. Scheifele (1998), The ACE magnetic fields experiment, *Space Science Reviews*, *86*, 613–632, doi:10.1023/A:1005092216668.

- Smith, E. J., and J. H. Wolfe (1976), Observations of interaction regions and corotating shocks between one and five au: Pioneers 10 and 11, *Geophysical Research Letters*, *3*(3), 137–140, doi:10.1029/GL003i003p00137.
- Snyder, C. W., M. Neugebauer, and U. R. Rao (1963), The Solar Wind Velocity and Its Correlation with Cosmic-Ray Variations and with Solar and Geomagnetic Activity, *Journal of Geophysical Research*, *68*, 6361, doi:10.1029/JZ068i024p06361.
- Temmer, M., B. Vršnak, and A. M. Veronig (2007), Periodic Appearance of Coronal Holes and the Related Variation of Solar Wind Parameters, *Solar Physics*, *241*, 371–383, doi: 10.1007/s11207-007-0336-1.
- Tsurutani, B. T., W. D. Gonzalez, A. L. C. Gonzalez, F. L. Guarnieri, N. Gopalswamy, M. Grande, Y. Kamide, Y. Kasahara, G. Lu, I. Mann, R. McPherron, F. Soraas, and V. Vasyliunas (2006), Corotating solar wind streams and recurrent geomagnetic activity: A review, *J. Geophys. Res. Space Physics*, *111*, A07S01, doi:10.1029/2005JA011273.
- Wanliss, J. A., and K. M. Showalter (2006), High-resolution global storm index: Dst versus SYM-H, *J. Geophys. Res. Space Physics*, *111*, A02202, doi:10.1029/2005JA011034.
- Webb, D. F., E. W. Cliver, N. U. Crooker, O. C. S. Cry, and B. J. Thompson (2000), Relationship of halo coronal mass ejections, magnetic clouds, and magnetic storms, *Journal of Geophysical Research*, *105*, 7491–7508, doi:10.1029/1999JA000275.
- Wu, C.-C., K. Liou, S. Plunkett, C. D. Fry, and S.-T. Wu (2013), Investigation of solar/heliospheric anomalies associated with the solar minimum of 2007–2008, *Terrestrial, Atmospheric & Oceanic Sciences*, *24*(2), 243–252, doi:10.3319/TAO.2012.10.16.01(SEC).
- Xu, F., and J. E. Borovsky (2015), A new four-plasma categorization scheme for the solar wind, *J. Geophys. Res. Space Physics*, *120*, 70–100, doi:10.1002/2014JA020412.
- Zhang, J., I. G. Richardson, D. F. Webb, N. Gopalswamy, E. Huttunen, J. C. Kasper, N. V. Nitta, W. Poomvises, B. J. Thompson, C. C. Wu, S. Yashiro, and A. N. Zhukov (2007), Solar and interplanetary sources of major geomagnetic storms ($Dst < -100$ nT) during 1996-2005, *J. Geophys. Res. Space Physics*, *112*, A10102, doi:10.1029/2007JA012321.
- Zhang, Y., W. Sun, X. S. Feng, C. S. Deehr, C. D. Fry, and M. Dryer (2008), Statistical analysis of corotating interaction regions and their geoeffectiveness during solar cycle 23, *J. Geophys. Res. Space Physics*, *113*, A08106, doi:10.1029/2008JA013095.
- Zhao, L., T. H. Zurbuchen, and L. A. Fisk (2009), Global distribution of the solar wind during solar cycle 23: ACE observations, *Geophys. Res. Lett.*, *36*, L14104, doi:10.1029/2009GL039181.